Effects of the Edges of 2D Materials on Photoelectrochemical Solar Energy Conversion

by

Tao Yan

A Dissertation

Submitted to the Faculty of

WORCESTER POLYTECHNIC INSTITUTE

In partial fulfillment of the requirements for the

Degree of Doctor of Philosophy

in

Materials Science and Engineering

by

April 2020

APPROVED:

Professor Pratap M. Rao, Advisor

Professor N. Aaron Deskins, Advisor

Professor Brajendra Mishra, Head of Program

Abstract

Research on renewable energy must be hastened to solve the energy crisis we are now facing. Among all sustainable energy sources, solar energy and hydrogen gas fuel are two of the most clean and powerful. Photo-electrochemical (PEC) reactions use solar energy to electrochemically split water to produce hydrogen gas. Photo-electrocatalyst materials play an important role in increasing the efficiency of PEC reactions by absorbing solar energy and directing the energy towards the desired electrochemical reactions.

Two-dimensional (2D) layered materials including MoS_2, WS_2, and SnS_2 have drawn considerable attention as electrocatalysts and photo-electrocatalysts because of the catalytically-active nature of their edges and high charge mobility and transport efficiency within their layers. This work focuses on the synthesis, measurement, and simulation of PEC properties and behavior of WS_2 nanotubes and SnS_2 nanoflakes.

The first part of this work focuses on experimental synthesis and PEC measurement of edge-on oriented WS_2 nanotubes and theoretical simulation of the atomic configuration and electronic structure of the edges by density functional theory (DFT) . WS_2 nanotubes were synthesized by chemical vapor deposition (CVD) and sulfurization, but showed very poor photresponse. The DFT simulation shows the edges of the WS_2 nanotubes are metallic, like those of 2H-MoS_2. The metallic edges likely act as recombination sites for photogenerated charges, which explains the poor photoresponse of WS_2.

The second part of this work focuses on experimental synthesis and PEC measurement of edge-on oriented SnS_2 nanoflakes and theoretical simulation by DFT.

The edge-on oriented SnS_2 nanoflakes exhibited high photoresponse and excellent PEC performance. The DFT simulation determined the atomic configurations of SnS_2 edges, and the stability of both bulk-like and monolayer SnS_2 edges at various S potentials. In contrast to WS_2 and MoS_2, the DFT simulation also determined that the edges of SnS_2 are semiconducting, not metallic. Therefore, the edges of SnS_2 would not cause recombination of photoexcited charges, and would enable SnS_2 to achieve a high photoresponse, as was experimentally observed. The DFT results also showed that the band gap energy of the SnS_2 edges becomes smaller with increasing sulfur coverage, and allowed the influence of chemical synthesis conditions on the electronic structure of the edges to be determined.

Acknowledgements

I would like to deeply acknowledge my first advisor, Professor Pratap M. Rao, and second advisor, Professor N. Aaron Deskins, for providing me the opportunity to work on the projects as a Ph.D. student. Without their constant guidance, support, patience, motivation, and encouragement, I could not arrive where I am now.

I would also like to express my appreciation to Professor Richard D. Sisson Jr., Professor Jianyu Liang, Professor Lybov Titova, who have provided excellent suggestion to this work as my thesis committee.

Special thanks to Doctor Boquan Li for his assistance on equipment training and maintenance. Special thanks to Rita Shilansky for helping me with daily routines.

My sincere thanks also goes to my labmates (Lite Zhou, Binod Giri, Yuhan Mei, Maryam Masroor Shalmani, Nicholas R. Pratt, Sunhao Liu, Jeremy Jacobs, and Adegite, Joseph O.) and friends (too many to list here, but you know who you are!) that I met here in WPI. I really cherish the time spending with them over my four-year research life in WPI. I could not have done this without their company, help, and support.

At last, I would like to appreciate my parents and other family members for their constant love and always supporting me without second thought.

Contents

List of Figures

List of Tables

Chapter 1

Introduction

1.1 Energy Challenges and Sustainable Energies

With 21st century coming into its third decades, the shortage of traditional energies, i.e. fossil fuels, are becoming more server. The non-renewability of the fossil fuels could drive prices up to the point that only a few people could afford. In addition, as people consume more and more fossil fuels, the global warming becomes more and more severe. Renewable energies are coming into people's sights because human realized that this may be the only way they will go out of the energy and environment crisis. Solar energy, wind energy, tidal energy, geothermal energy, and bio mass, all of these give perfect ideals of sustainable and environment friendly development. However, in 2019, the majority of energy recourse was still fossil fuels, which reminds people to speed up whatever they can and find the practical way to go out of the energy crisis.

1.1.1 Traditional Energies

Fossil fuels (coal, oil, and natural gas) has been dominate energy source world wide since the Industrial Revolution in the 18th to 19th century. The data from Our World in Data by University of Oxford (Figure 1.1(a)) [1] shows that coal was the only energy source until the late 18th century when crude oil consumption started. Natural gas consumption began couple decades later than crude oil did. Started from late 19th century, crude oil has been the largest energy source. Till 2017, crude oil account for around 40% of fossil fuel, followed by coal and natural gas accounting for around 32% and 27%, respectively.

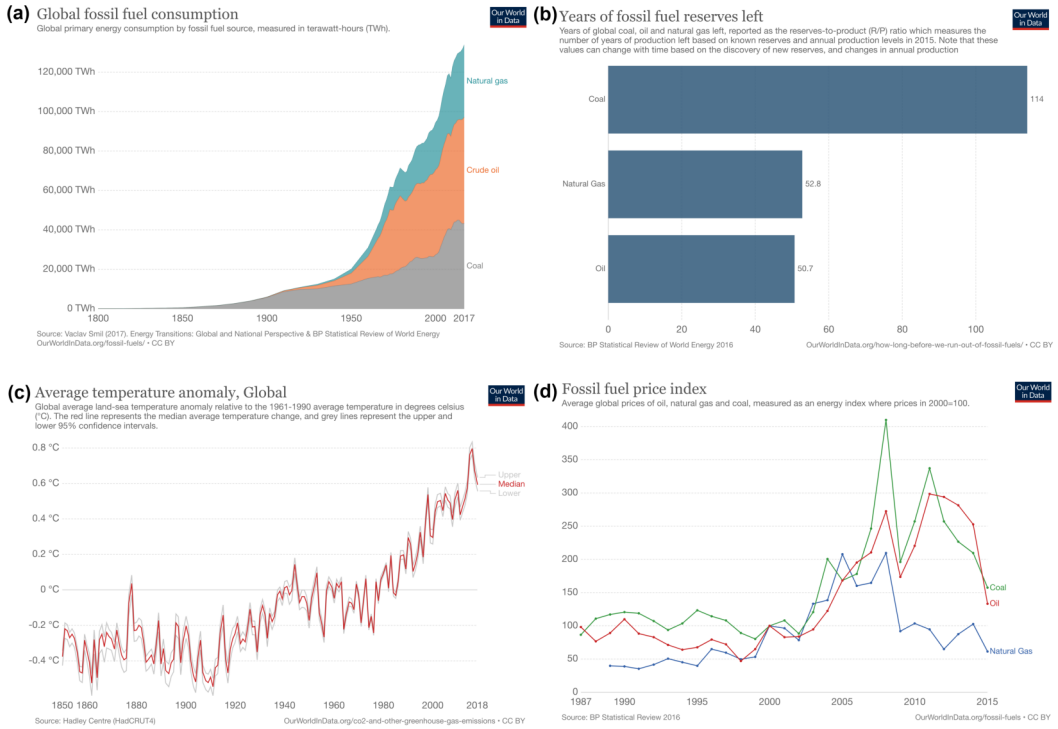

Figure 1.1: (a) Global fossil fuel consumption from 1800 to 2017.(b) Years of fossil fuel reserves left relative to known reserves and production in 2015.(c) Global average temperature anomaly from 1850 to 2018. (d) Fossil fuel price index from 1987 to 2015. The value of 2000 was set as 100.

As is well known that fossil fuels are almost not renewable. Once they are

used up, it will take tens of thousands years of the nature to recover. The data in Figure 1.1 (b) shows the year of coal reserves left since 2015 is 114, and that of natural gas and oil is around half century only. This is an upset data which tells us that human would use up all fossil fuel in the next two generations. If human beings keep wasting and not looking for new energy resources, human would face a harsh time in the not far future.

In addition to the shortage of the fossil fuels, by-products such as carbon dioxide (CO_2) generated by consumption of the traditional energies are not environmental friendly either. Because of greenhouse gases emission, the global average temperatures have increased by over one degree Celsius since 1860s according to Figure 1.1 (c). The average temperatures have risen sharply in recent years, which makes Global Warming more sever. Climate changes have a large number of negative affects such as extreme weather events, see-level rise, altered crop growth, and diseases.

Because of all these factors above, the price of fossil fuel could be very high that only a few people could afford. The price of Coal and oil have increased more than 2.5 times today than 2000, although the price of natural gas does not rise that much (Figure 1.1 (d).

All in all, there is a urgent requirement of looking for clean and sustainable energy resources to replace fossil fuels in the future.

1.1.2 Sustainable Energies

Replacement of fossil fuels with sustainable energy resources is one of biggest challenges human have to face in the 21st century. Luckily, multiple clean energies have been found already and the most of them are out their producing electricity, heating, and other energies needed in the daily life. These sustainable energies including

solar, wind, tidal, bio-mass, and geothermal energy.

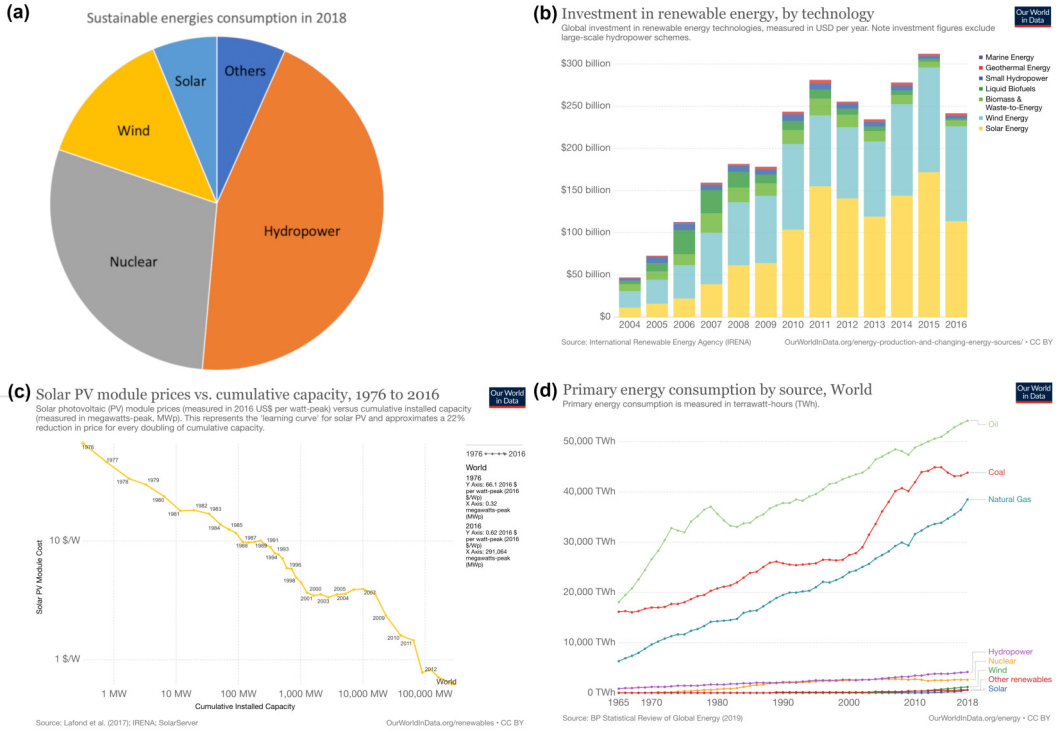

Figure 1.2: Sustainable energies developments. (a) Consumption of different sustainable energies in 2018; (b) Investment in sustainable energies from 2004 to 2016; (c) Prices of PV panels from 1976 to 2016; (d) Global primary energy consumption by source including traditional and sustainable energies. All data are from Our World in Data by University of Oxford [1].

Hydropower consumption accounts for 2.7% of total global energy consumption in 2018, which is also the highest among all renewable energies (see Figure 1.2 (a)) [1]. Hydropower supplied 16% of electricity all around the world in 2015 [2]. Right behind hydropower, nuclear consumption accounts for 1.7% of total global energy consumption in 2018. Nuclear power plant was once considered the most dangerous electricity power plant, but after statistic analysis nuclear power actually is the safest energy source. Contrary to people's common thoughts, the death rate of nuclear power production is way less than that of fossil fuels, even taking into consideration of the Chernobyl (1986) and Fukushima Daiichi (2011) disasters [2].

Wind power is another clean energy which produced 6% of global electricity in 2018 (data came from Global Energy Statistical yearbook 2019). From Figure 1.2(b) we can see that the investment of wind energy and solar energy are the highest two energies among all sustainable energies.

Solar energy is the light and radiant from the sun. It can be converted to electricity, heat, chemical potentials, etc. through various coversion system. It is sustainable and few byproducts as well. Although the efficiency of solar energy conversion is much lower than that of fossil fuels; plus the price of photovoltaic (PV) panels are quiet pricey for now, through years of development the efficiency is increasing a lot and the price of PV panels has reduced 22% since 1976 (Figure 1.2(c)).

The sustainable energies are clean, safe, and renewable, but the most of them are low efficient and not cheap, which is the main reason that fossil fuels are still the major energy source human is using now. Figure 1.2(d) compares primary energy consumption through 1965 to 2018. One can see that sustainable energy is only a mall portion of the total global energy people use every year. To improve the performance and price of sustainable energy source is two main goals of scientists, so that the traditional energy sources are not in need anymore and improve the environments of the earth.

1.2 Photoelectrochemical Water splitting

Among the sustainable and renewable energy sources, hydrogen may be the cleanest and have largest specific energy (the amount of energy per mass). Hydrogen production requires only water and electricity, no carbon emission. In fact, NASA has used liquid hydrogen since the 1970s to propel the space shuttle and other rockets in space. Those hydrogen fuel cells drive the shuttle's electrical systems, producing

a clean byproduct – pure water, which the crew drinks. The specific energy of H_2 is around 142 MJ/kg [3], while the maximum of traditional fossil fuels is only 55.5 MJ/kg. Besides, hydrogen fuels could store and transport energy easily, making H_2 a very promising renewable energy resources. These years there are more and more Hydrogen fuel cell cars which provides as good engine as traditional cars but less pollution.

Making hydrogen then is one of critical projects. Water splitting (Figure 1.3(a)) produces H_2 by splitting H_2O through photo-electrochemical or electrochemical reaction with O_2 as main byproduct. It is consist of two half reactions - water oxidation (anodic reaction) and reduction (cathodic reaction):

$$2H_2O + 4h^+ \rightarrow O_2 + 4H^+, \tag{1.1}$$

$$2H^+ + 2e^- \rightarrow H_2. \tag{1.2}$$

Reaction 1.1 happens at the cathode where water is oxidized to O_2 through oxygen evolution reaction (OER) and reaction 1.2 happens at the anodes where H^+ ion accepts electron and produces H_2 gas through hydrogen evolution reaction (HER). There is a 237 kJ/mol [4] or 2.456 eV of energy barrier to drive the reaction happen (Figure 1.3(b)).

However, the experimentally observed potential is larger than the thermadynamically determined potential, i.e. 2.456 eV of the reaction, 1.23 eV of each half reaction. The difference of the potential called overpotential. Catalysts are now showed up to reduce the overpotential and improve the energy conversion efficiency as well. There are two types of catalysts: photo-electrocatalysts and electrocatalysts. They are both semiconductors with proper bandgaps that align with HER and OER potentials. As shown in Figure 1.3 (a), for cathode catalysts (usually

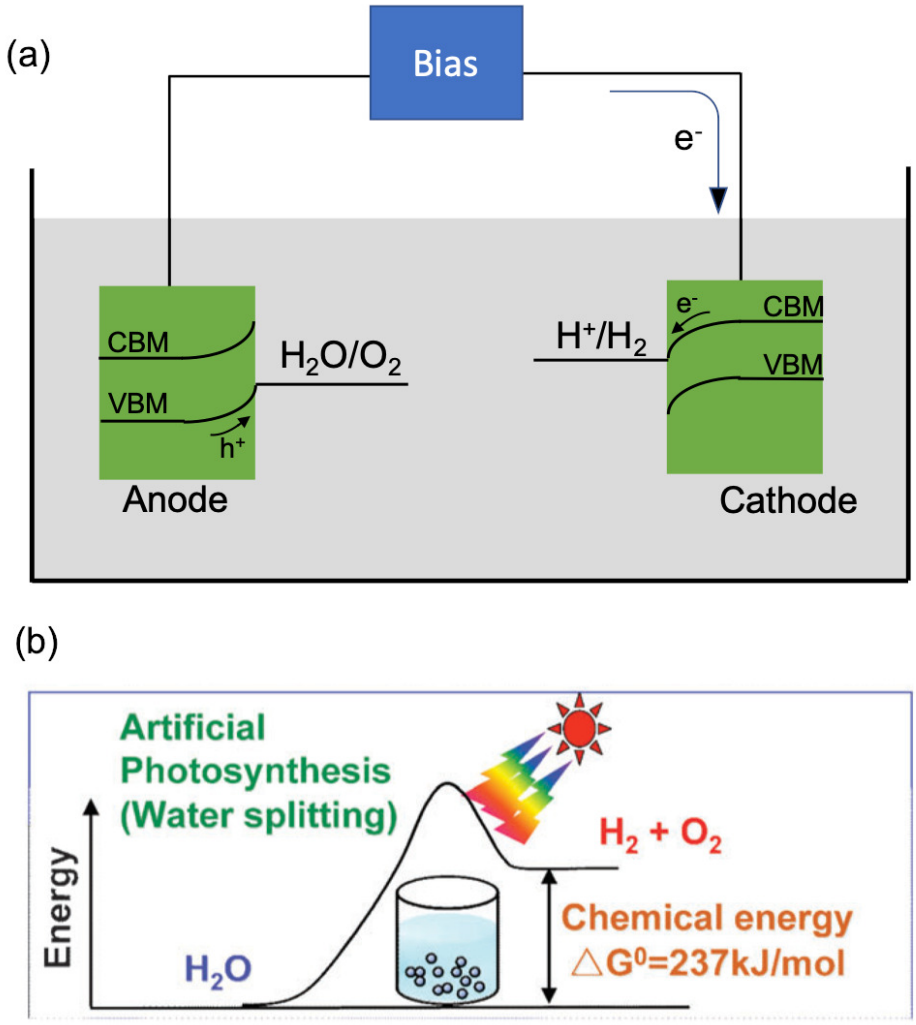

Figure 1.3: A simple Water splitting reaction setup (a), and the energy barrier of the reaction schematic diagram (b) [4].

are p-type semiconductors), the conduction band minimum (CBM) should be more negative than HER potential while the valence band maximum (VBM) of anode catalysts (usually are n-type semiconductors) is required to be more positive than OER potential. An external bias/voltage can be used to drive electrons to the counter electrode, improving charge separation.

The processes of photoelectrochemical water splitting is quite similar to photosynthesis [4]. It has three major steps. The first step is photon absorption. The

second step is diffusion and recombination of electrons and holes. The last step is surface chemical reaction. The next few sections talk about the photoelectrochemical water splitting step by step in details.

1.2.1 Photon absorption

As mentioned in previous section, photoelectrocatalysts are semiconductors with proper band gap energy. When the energy of incident light/photon is larger than the energy of the band gap, electrons in valence band can absorb the light energy and are excited to conduction band leaving equal number of holes in the valence band. When sunlight reaches photoelectrocatalysts after going through atmosphere and/or electrolyte, one part of it is reflected by the surface of the catalysts, one part of it is absorbed, and one part of it transmit the catalysts.

Light absorption intensity

The absorption coefficient (α_λ) is used to determine the depth of a light with certain wavelength (λ) penetrating the material before it is absorbed. If a material has small absorption coefficient, the light absorption depth is large, meaning the materials is not a good light absorper. Then the material is more likely to be transparent. When the incident light is perpendicular to the surface, then the intensity of transmission is described by equation

$$I(trans)_\lambda = I_0 e^{-\alpha_\lambda l} \tag{1.3}$$

where I_0 is intensity of incident light, l is penetration depth (i.e. the thickness of the material). Then the intensity of light absorbed is described by the following equation ignoring reflection light:

$$I(ab)_\lambda = I_0(1 - e^{-\alpha_\lambda l}) \tag{1.4}$$

Single semiconductor usually has different absorption coefficients for different wavelength, but generally it has larger absorption coefficient at shorter wavelength than at longer wavelength.

Semiconductors with direct band gap are stronger light absorption than those with indirect band gap. Electrons in the valence band gap absorb only photon to jump to conduction band in direct-bandgap semiconductors, while the electrons also absorb phonon in indirect-bandgap semiconductors. Because phonons can transfer momentum to electrons.

Efficiency

For semiconductors the maximum absorption efficiency depends on the band gap energy. For example, the maximum absorption efficiency of intrinsic TiO_2 is less than 4%, because the band gap energy of TiO_2 is 3.2 eV which means it is only able to absorb the wavelength large than 3.2 eV of sun light.

In the PEC water splitting, incident phonton to electron conversion efficiency (IPCE) is one of the factors that determine the performance of the photoelectrocatalytic activity of a catalyst. IPCE can be calculated by

$$\mathrm{IPCE}(\lambda) = \frac{1240[\mathrm{voltnm}] \times J[\mathrm{mAcm^{-2}}]}{P_\lambda[\mathrm{mWcm^{-2}}] \times \lambda[\mathrm{nm}]} \times 100\%, \tag{1.5}$$

where J is the current density at certain wavelength (λ), P_λ is the intensity of incident light with λ wavelength.

1.2.2 Charge transport and recombination

The photogenerated electrons and holes then transport to the opposite directions due to drift and diffusion. The photogenerated charge carriers drift along electric

field. The current density therefore is called drift current which can be described as

$$J_{total}(drift) = J_n(drift) + J_p(drift) = q(n\mu_n + p\mu_p)E, \tag{1.6}$$

where $J_i(drift)$ is drift current density of i particle (electrons, holes, or total);q is the quantity of electric charge; n and p are the number of electrons and holes; μ_n and μ_p are corresponding mobility of electrons and holes; and E is electric field (including external bias and quasi-Fermi energy). The mobility of carriers is a measure of ability of carrier drift in response to electric field. It is affected by the carrier's weight, temperature, concentration, etc. If the weight of carrier is large, the mobility is small. If the temperature is high, the mobility is small. If the concentration of the carrier is high, the mobility is also small because the collision among carriers happens more often when the concentration of carrier is higher.

Besides drift, diffusion is another carrier movement involved in carrier transport. Diffusion is the movement of carrier in response to carrier concentration gradient. Similarly, the current density generated by carrier diffusion is called diffusion current, which can be described as

$$J_{total}(diff) = J_n(diff) + J_p(diff) = q(D_n\frac{\mathrm{d}n}{\mathrm{d}x} - D_p\frac{\mathrm{d}p}{\mathrm{d}x}), \tag{1.7}$$

where D_n and D_p are diffusion coefficient of electrons and holes. Diffusion coefficient, similar to mobility, is a measure of ability of carrier diffuse in response to a concentration gradient. It is effected by vibration of atoms in the semiconductor. Therefore the total current density is

$$J_{total} = J(drift) + J(diff). \tag{1.8}$$

Ideally, all photogenerated electrons and holes are able to transport to charge collectors, but due to the imperfections of materials and the nature of electrons and holes there are somewhat recombination before the charges arrive charge collectors. If the photogenerated electrons recombined with holes crossing the band gap, the recombination is called direct recombination. During the charge recombination, there is the energy release which results in light/phonon emission. Direct recombination is also known as radiative recombination, which dominates in semiconductors with direct band gaps. The direct recombination rate for n-type semiconductors is described as

$$U = \frac{p - p_0}{\tau_{p,direct}}, \tag{1.9}$$

where p is the total number of holes with light shining, p_0 is the number of holes in the dark, and $\tau_{p,direct}$ is the average life time of holes which can be described as

$$\tau_{p,direct} = \frac{1}{\beta n_0}, \tag{1.10}$$

where β is direct recombination constant. Likewise, the direct recombination rate for p-type semiconductors is

$$U = \frac{n - n_0}{\tau_n}, \tag{1.11}$$

where n is the total number of electrons with light shining, n_0 is the number of electrons in the dark, and τ_n is the average life time of electrons. One can see that the direct recombination rate is limited by minority carrier.

Another recombination mechanism is indirect recombination. There is sometimes trap states within the band gap that capture photogenerated electrons or holes and the opposite charge carrier can also occupy. This type of recombination is known as Shockley-Read-Hall (SRH) recombination or defect recombination. The

intermediate states within the band gap result in lower energy release. Different from light emission during direct recombination, the energy released during indirect recombination is in form of thermal energy. The indirect recombination rate for n-type semiconductors can be described by Shockley-Read-Hall equation:

$$U = \nu\sigma N_t \Big[\frac{n_0 p - n_0 p_0}{n_0 + p + 2n_i \cosh(\frac{E_t - E_{Fi}}{kT})} \Big]. \tag{1.12}$$

ν is thermal velocity. σ is trap cross section area. N_t is trap concentration per volume. E_t is energy level of trap. E_{Fi} is intrinsic Fermi energy level. k is Boltzmann constant. T is temperature. It can be simplified as

$$U = \frac{p - p_0}{\tau_{p,indirect}}. \tag{1.13}$$

The average life time of holes in the indirect recombination, $\tau_{p,indirect}$, can be described as

$$\tau_{p,indirect} = \frac{1}{\nu\sigma' N_t}, \tag{1.14}$$

where σ' is effective capture cross-section. The indirect recombination rate For p-tye semiconductors is similar to equations from equation1.12 to equation1.14:

$$U = \frac{n - n_0}{\tau_{n,indirect}}, \tag{1.15}$$

where

$$\tau_{n,indirect} = \frac{1}{\nu\sigma' N_t}. \tag{1.16}$$

Auger recombination is another major charge recombination type. There are three charges involving in Auger recombination. The energy released by photo-generated electrons dropping back to valence band does not result in light or heat

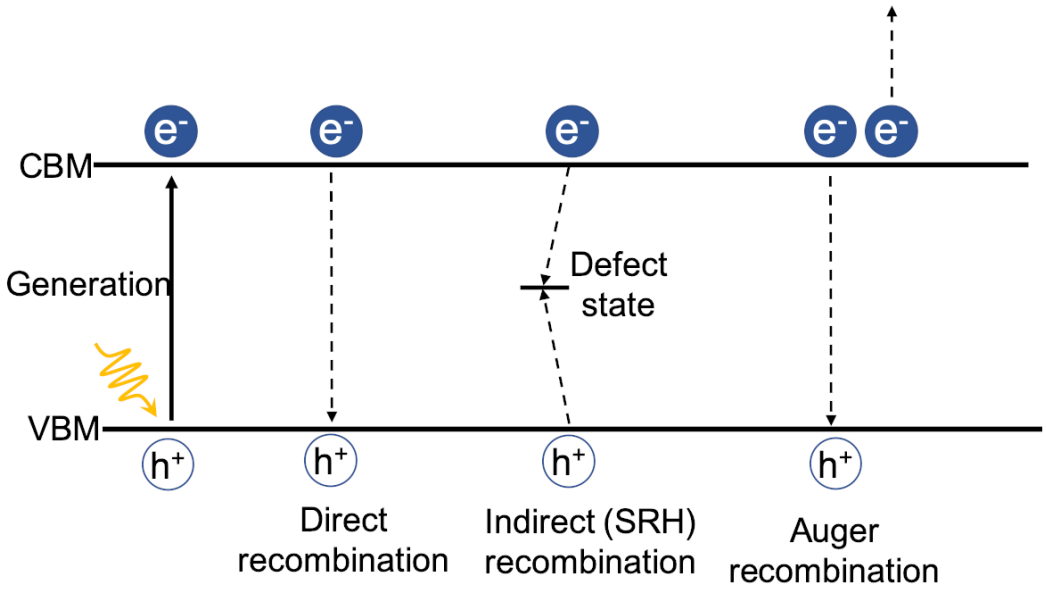

Figure 1.4: Charge recombination types.

emitting, but results in another electron in the conduction band jumping to higher energy level. This electron would thermalize back to conduction band edge afterwards. Auger recombination is essential in the semiconductors that are heavily doped. The recombination rate of Auger recombination is similar to direct recombination except includes the energy that the electron in the conduction band received from recombination. So it can be described as

$$U = \frac{p - p_0}{\tau_{p,Auger}}, \tag{1.17}$$

where average life time of holes in Auger recombination is

$$\tau_{p,Auger} = \frac{1}{C_n n_0^2}. \tag{1.18}$$

C_n is Auger recombination constant.

Figure 1.4 summarizes all three major charge recombination types above. Dan-

gling bonds at materials surface also create traps that increase the charge recombination rate. The rate of surface recombination for n-type semiconductors can be calculated by:

$$U = S(p - p_0), \tag{1.19}$$

where surface recombination velocity S is described as

$$S = \mu\sigma'_S N_{st}. \tag{1.20}$$

N_{st} is concentration of surface traps. The surface morphology and atomic configuration of the catalyst can determine the surface recombination rate. Fortunately, in PEC water splitting, surface recombination can be decreased by passivation.

1.2.3 Surface chemical reaction

The last step of PEC water splitting is surface chemical reaction. This is the step where the HER takes place (reactions 1.2). The reaction involves two steps (Figure 1.5). Forming of bonds between hydrogen and the catalyst is the first step [5]:

H^+ e^- + catalyst-surface $\rightarrow$ catalyst-H.

The second step is the release of hydrogen molecules through one of the two processes:

2catalyst-H $\rightarrow$ H_2 + 2catalyst-surface (The left loop in Figure 1.5)

or

$H^+ + e^-$ + catalyst-H $\rightarrow$ H_2 + catalyst-surface (The right loop in Figure 1.5).

The two Hydrogen atoms recombination is the rate-controlling step in the HER at Pt, the best HER catalyst by now, because the change in Gibbs free energy is uphill at zero applied voltage [6]. The electrochemical HER reaction is driven by an applied voltage that supplies both the thermodynamic free energy for the reaction

to occur, and also the additional energy required to drive the reaction over kinetic barriers.

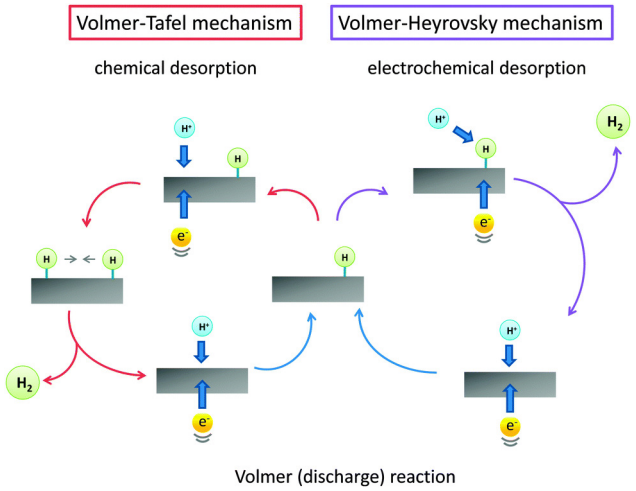

Figure 1.5: Mechanism of HER on the surface of an catalyst in acidic solutions [7]

The rate of hydrogen evolution reaction is proportional to the electrical current passing through the catalytic electrode. The relationship between the current and applied voltage is called the current-overpotential equation, which can be written as:

$$\eta = A\ln(\frac{i}{i_0}) \tag{1.21}$$

where η is overpotential, A is called Tafel slope, i is current and i_0 is exchange current density. Overpotential, as briefly mentioned in Chapter 1.2, is the difference of voltage applied to the electrode and the redox potential (H^+/H_2 in this case) in the electrolyte. It is an essential energy to drive the HER and OER.

Tafel slope and exchange current density are the two critical parameters to evaluate the activity of electrocatalysts. Tafel slope indicates how much potential is needed to increase or decrease the current density by 10-fold [8]. Theoretically, the Tafel slopes equation has three limiting conditions [9]. (1) If the discharge step is fast and the HER reaction is determined by H-H combination, a slope of 29 mV/decade

should be observed at room temperature. (2) If the discharge step is fast and the HER reaction is determined by ion$^+$ atom reaction, the Tafel slope should be 38 mV/decade at room temperature. (3) If the discharge step is slow, the Tafel slope should be 116 mV/decade at room temperature. Exchange current density is the current under zero overpotential which is also under reversible conditions [7]. The value of exchange current density is a measure of the catalytic activity of the active sites, and therefore influences the rate of the catalytic reaction. To have higher electrocatalytic activity of HER, the catalysts should achieve the largest exchange current density and the lowest Tafel slope.

1.2.4 PEC water splitting materials

In 1972 scientists firstly shone UV light to a semiconductor electrode, n-type TiO_2 (rutile), connected to Pt counter electrode with a bias [10] resulting in first photoelectrocatalysis. A number of scientists had extensively studied PEC since the finding. Metal oxides such as ZnO [11, 12], Fe_2O_3 [13], WO_3 [14], $BiVO_4$ [15], metal sulfides such as CdS [16], SnS_2 [17], nitrides such as GaN [18], C_3N_4 [19], and heterojunction photocatalysts [20], etc. have been studied in photoelectroncatalysis area for years.

Metal oxides

Metal oxides are the most popular photoelectrocatalysts on PEC water splitting due to their high stability, proper band gap energy and position. Two major metal oxides photoelectrocatalysts that also have highest performance are TiO_2 based and hematite (α-Fe_2O_3).

TiO_2 can only be excited by ultra-violet (UV) irradiation which accounts for only 4% of solar spectrum [21], because of its wide band gap energy (3.2 eV). Be-

sides, one important barrier for PEC performance of TiO_2 is the rapid recombination rate. Therefore by changing the nanostructure of TiO_2, some researchers are trying to improve its PEC performance. Such as TiO_2 nanotubes [22, 23], nanowires [24], TiO_2/Si core/Shell nanowires [25], etc. There are also some researchers focused on addition of sacrificial reagents and carbonate slats to avoid high recombination rate [26, 27]. Other researchers focused on metal loading [28, 29, 30], ion doping [31], dye sensitization [32, 33], etc. to enhance the absorption efficiency of the photoelectrocatalyst. TiO_2 nanotube arrays has the highest efficiency among all TiO_2 based PEC cells [23]. The overall conversion efficiency is 6.8%, and photocurrent is around 16 mA/cm^2 at 0 V vs. Ag/AgCl.

Hematite (α-Fe_2O_3) has relative smaller band gap energy (around 1.9 to 2.2 eV) and quite stable in aqueous solution, which makes it is a good caditite of photoelectrocatalyst. However, the low efficiency and large overpotential limited the direct usage. Surface treatment, such as a monolayer Co^{2+} coated on the surface of hematite [34] results in higher photocurrent and lower overpotential, and nanostructure control such as mesoprous thin films [13, 35] and Fe_2O_3 naowire arrays [36]. Hematite with cobalt monolayer on top has the highest PEC performance with 2.7 mA/cm^2 photocurrent at 1.23 V_{RHE} and IPCE = 42% at 370 nm [34].

Metal sulfides

Metal sulfides such as CdS_2,and SnS_2 have been studied as photoelectrocatalysts, because of their around 2.2 eV of band gap energy is suitable for visible light absorption. However, CdS_2 and SnS_2 are not as stable as metal oxides in the aqueous solutions, extra treatment or cooperate with other semiconductors are necessary.

CdS is attractive because its band gap straddle the HER and OER potentials as well as suitable for visible light absorption (band gap energy is around 2.2 eV).

However, the poor stability and high charge recombination rate of CdS limited its application in PEC water splitting. Therefore, the synthesis of heterojunction of CdS with other semiconductors has been studied such as TiO_2/CdS [37, 38], PdS/CdS [16], ZnO/CdS [39]. Among these, the cobalt phosphate water oxideation (Co-Pi WOC) catalyst stabilized, CdS sensitized TiO_2 nanowire array has the highest photocurrent, 8 mA/cm^2 at 0V vs. Ag/AgCl with IPCE = 55% at 400 nm [37]. In this case, CdS is light absorber due to its relative narrow band gap energy, while TiO_2 provides a pathway for transport of electrons. However, Cd and its compounds are highly toxic. The Cd-based PEC catalysts are not likely to be commercialized.

SnS_2 has the similar band gap energy as CdS, 2.3 eV, which makes it also suitable to absorb visible light. Besides, SnS_2 has a very high carrier mobility. The best PEC performance of SnS_2 is SnS_2 nanoflakes made in our group by close space sublimation (CSS), which has 4.5 mA/cm^2 photocurrent at 1.23 V_{RHE} and 70% front IPCE [17]. This topic is discussed more in details in Chapter 1.3 and Chapter 3.

Nitrides

Nitrides were studied for visible light PEC water splitting for decades due to the proper band gap energy. Since nitrides alone perform very poor photoelectric activity for water splitting, co-catalysts or heterojunctions were made to improve performance [20]. For example, pristine g-C_3N_4 has band gap energy of 2.7 eV, and the band gap straddle HER and OER potentials, which leads to potential application for visible light water splitting. g-C_3N_4 also has high resistance in strong acid, strong alkaline, and high temperature, but the high charge recombination rate leads to negative water splitting performance. g-C_3N_4 based junctions such as g-C_3N_4/graphene [40] exhibited more than 3 times photocurrent than g-C_3N_4 alone. However, the highest photocurrent of g-C_3N_4 based junction is only 1.5 mA/cm^2 at

1.23 V_{RHE} with IPCE = 40% at 400 nm [41]. Other nitrides such as RuO_2 loaded β-Ge_3N_4 [42, 43] and GaN [43], metal ion doped GaN [18, 44], etc. shows potential ability for overall water splitting. All in all, similar to metal sulfides PEC water splitting materials, there are not many reports on nitrides PEC water splitting. Mostly because of their poor performance (low photocurrent, low efficiency, high recombination rate, etc.), though their band gap energy and positions are suitable for the application.

Summary

Table 1.1 summarizes the several materials that have relative high performance for PEC water splitting. Basically, metal oxides are the most promising PEC catalysts due to their high stability in aqueous solution and relatvie high performance. However, the oxides has very low sun light absorption efficiency due to their larger band gap energies. Therefore, materials that has narrow band gaps are attractive recently. Nitrides have proper band gap energy to absorbe visible sun light, but the photocurrent and solar-to-chemcial conversion efficiency of the nitrides alone are not comparable. Some sulfides such as SnS_2 nanoflake has found has comparable properties such as proper band gap energy and high intrinsic mobility, but more effort is needed on searching and studying their PEC water splitting.

Table 1.1: Summary of PEC water splitting materials and their performance.

Materials	photocurrent	efficiency	reference
TiO_2 nanotube	13 mA/cm^2 at 0 V vs. Ag/AgCl	IPCE > 90 at 337 nm	[23]
Fe_2O_3-Co	2.7 mA/cm^2 at 1.23 V_{RHE}	IPC=36% at 400 nm	[34]
TiO2/CdS	6.5 mA/cm^2 at 0 V vs Ag/AgCl	IPC=45% at 400 nm	[38]
ZnO/ZnS/CdS/$CuInS_2$	10.5 mA/cm^2 at 0 V vs Ag/AgCl	IPCE=57.7% at 480 nm	[45]
ZnSe monolayer	0.3 mA/cm^2 at 0 V vs Ag/AgCl	IPEC = 5% at 400nm	[46]
SnS_2 nanoflakes	4.5 mA/cm^2 at 1.23 V_{RHE}	IPCE=70% at 400 nm	[17]
CoOx/C_3N_4/WO_3	1.5 mA/cm^2 at 1.23 V_{RHE}	IPCE = 40% at 400 nm	[41]
WO_3 nanowire	1.43 mA/cm^2 at 1.23 V (two-electrode method)	IPCE=60% at 400 nm and 0.5 V	[47]

1.3 Two-dimensional (2D) Materials

Two-dimensional (2D) materials has been popular for decades since graphene was first isolated in 2004. Nobel Prize in Physics was awarded to Andre Geim and Konstantin Novoselov for showing the unusual properties of graphene in 2010 [48]. 2D materials have multilayered structure, in which the layers are hold together by van der Waals forces, while within each layers there are chemical bonds holding atoms together. Because of the wake van der Waals interaction between each layer, there is always some methods to isolate a single layer from the bulk material. The unique structure, property, and earth abundance of 2D materials therefore make them of interests for decades.

Some 2D materials are metallic or even superconducting such as NbS_2, $NbSe_2$, TaS_2, and $TaSe_2$. Many more 2D materials have been discovered and studied on photoelectrocatalysis and electrocatalysis in recent years including graphene, previously mentioned g-C_3N_4, transition metal dichalcogenides (TMDs) such as MoS_2, $MoSe_2$, $MoTe_2$, WS_2, and WSe_2, and SnS_2, etc. Due to the multilayered structure, 2D materials provides more reaction sites for catalytic reaction; and the photogenerated electrons and holes can transport along chemical bonds, which improves the efficiency of photon-to-electron conversion. In addition, there are a number of 2D materials that are earth abundance and non-toxic. While some 2D materials, such as MoS_2, have better performance on electrochemicial water splitting due to high charge recombination rate at the surface. Applications of several TMDs including MoS_2 and WS_2 and SnS_2 are discussed in this section. At the end of this chapter several unique properties and applications of the three materials for a comparison were tabulated in Table 1.1.

1.3.1 Optoelectronic applications

PEC water splitting

As for PEC water splitting, only SnS_2 has promising performance among the three materials, probably due to the fast carrier recombination rate at the metallic edges of MoS_2 and WS_2. Vertical orientated SnS_2 nanoflakes are proven have 2 times larger photocurrent than horizontal nanoflakes [49]. Vertical SnS_2 nanoflakes were synthesized with close space sublimation in 2019. Each nanoflake was a combination of thinner flakes with different lengths, which makes more edges, i.e. active sites, exposed. These step-layered SnS_2 nanoflakes achieved the as high as 4.5 mA/cm^2 photocurrent in Na_2SO_3 electrolyte, which is the highest photocurrent of SnS_2 for now [17].

Photodectors

Due to their high carrier mobility as well as the proper band gap energies, MoS_2, WS_2 and SnS_2 have been studied for photodetectors/phototransistors. MoS_2 was found as a good photodetector materials because of the band gap energy of it is around 1.5 eV, the carrier mobility is 200 $cm^2/V/s$ [50, 51] and 0.1 - 0.1 ns of photoexcited carrier life time [52, 53]. Monolayer MoS_2 photodector with a ferroelectric gate has a as short as 1.8 ms response time and more than 2000 A/W photoresponsivity [54]. While the intrinsic carrier mobility of SnS_2 (330 $cm^2/V/s$) is higher than that of MoS_2 and 1.3 ns of photoexcited carrier life time [17], the shortest response time of SnS_2 photodector is only around 5 μs [55]. WS_2 alone is not comparable with MoS_2 and SnS_2 on photodectors, but MoS_2/WS_2 heterojunction array has 2.3 A/W responsivity [56].

1.3.2 Electrical applications

EC water splitting

The most efficient HER catalyst for now is Pt which, however,is a expensive material. Edge-rich MoS_2 has been studied for decades because the hydrogen adsorption energy of MoS_2 edges has been found is less than 0.2 eV [5] meaning potential high HER performance. Vertical aligned MoS_2 layers have 2.2 $\times 10^{-6}$ A/cm^2 exchange current density, which is very close to theoretical prediction (7.9 $\times 10^{-6}$ A/cm^2) [57], and 75 mV/decade Tafel slope which is slightly higher than prediction (55 mV/decade). This is very close to Pt whose exchange current density is around 4.5 $\times 10^{-4}$ A/cm^2 among 2D materials HER catalysts.

Although WS_2 has similar crystal structure as MoS_2, there are few reports studying HER performance of WS_2. WS_2 achieved similar or slightly better HER performance than MoS_2 when loaded WS_2 on carbon cloth electrode [58]. 68 mV/decade of Tafel slope and 5.8 $\times 10^{-6}$ A/cm^2 of exchange current density. However the synthesis condition of the WS_2 is very harsh and the procedure is quite complicated. SnS_2, on the other hand, is not quite stable on photocathode usage.

Field-effect transistors (FETs)

Transistor is a important application for semiconducting materials in digital electronics. The current state-of-the-arit field-effect transistors (FETs) are silicon-based metal-oxide-semiconductor FETs. Reduction of scale is a important project for FETs facing smaller device and the heat dissipation issue. 2D materials semiconductors have high carrier mobility and can be isolated to few layers or monolayer layer with few nanometer thick, therefore draw lots of interests as channel materials in recent years. Monolayer SnS_2 FETs with carrier mobility of 50 cm^2/V/s has a

more than 10^7 on/off ratio (the ratio of on-state to off-state conductance) [59]. MoS_2 FETs with carrier mobility of 0.1-10 $cm^2/V/s$ has a 10^8 on/off ratio [50]. Monolayer WS_2 FETs was achieve as high as 83 $cm^2/V/s$ of mobility [60].

1.4 Density Functional Theory (DFT)

Density functional theory (DFT) is a tool to calculate properties and energies of materials through calculating electron density and electron wave functions with quantum chemistry theory [61, 62, 63]. Start from 1900s, scientists studied structure, density and wave functions of electrons. In the mid-1960s Kohn and Hobenberg proved two fundamental mathematical theorems for density functional theory [64] followed by numerous scientists who joined the development of DFT. Until now, the best approach to simulate and calculate the electron wave function that Kohn provided has not been developed. This part of work is a short summary of one part of the theory of DFT. See this reference [63, 65] for more information and details if interested.

1.4.1 Theoretical background

The Schrödinger equation

One simple form of the Schrödinger equation that people may familiar with is $H\psi = E\psi$, where H is the Hamiltonian operator, ψ is a set of solutions, or eigenstates, of the Hamiltonian, and E is eigenvalues associate with each solution of ψ_n. To describe molecules, a more complicated form is

$$\Big[-\frac{\hbar^2}{2m} \sum_{i=1}^{N} \nabla_i^2 + \sum_{i=1}^{N} V(\vec{r}_i) + \sum_{i=1}^{N} \sum_{j<1} U(\vec{r}_i, \vec{r}_j) \Big] \psi = E\psi. \tag{1.22}$$

The three terms in brackets are, in order, the kinetic energy of each electron, the interaction energy between each electron and the collection of atomic unclei, and the interaction energy between different electrons. $\vec{r}$ is the electrons position. ψ is electronic wave functionwhich can be written in terms of the individual electron wave functions as

$$n(\vec{r}) = 2\sum_i \psi_i^*(\vec{r})\psi_i(\vec{r}) \tag{1.23}$$

Hohenberg-Kohn theoroms and Kohn-Sham equations

As mentioned above that the entire density functional theory field is based on two theorems provided by Hohenberg and Kohn (the HK theorems). The first one is "the ground-state energy from Schrödinger's equation is unique functional of the electron density". In other words, the ground-state electron density uniquely determines all ground-state properties. And the second HK theorem is " the electron density that minimizes the energy of the overall functional is the true electron density corresponding to the full solution of the Schrödinger equation". This means by varying electron density one could find the minimum energy and therefore the "true" electron density associated with the Schrödinger equation can be found.

Based on the HK theorems, Kohn and Sham derived the Schrödinger equation for DFT:

$$\Big[-\frac{\hbar^2}{2m}\nabla_i^2 + V(\vec{r}) + V_H(\vec{r}) + V_{XC}(\vec{r})\Big]\psi_i(\vec{r}) = \varepsilon_i\psi_i. \tag{1.24}$$

The main difference bewteen Kohn-Sham equation and equation 1.22 is that Kohn-Sham equations are single-electron wave functions, so that there are missing summations in the Kohn-Sham equations. The last term in the brackets is the unknown term called exchange-correlation energy.

exchange-correlation functional

To solve Kohn-Sham equations one have to define exchange-correlation functional. Although this is the part that have not been 100% figured out, there are a number of functional to calculate exchange-correlation energy. Figure 1.6 shows a exchange-correlation functional ladder that includes several normal exchange-correlation functional researchers are using in their daily research in the order of accuracy.

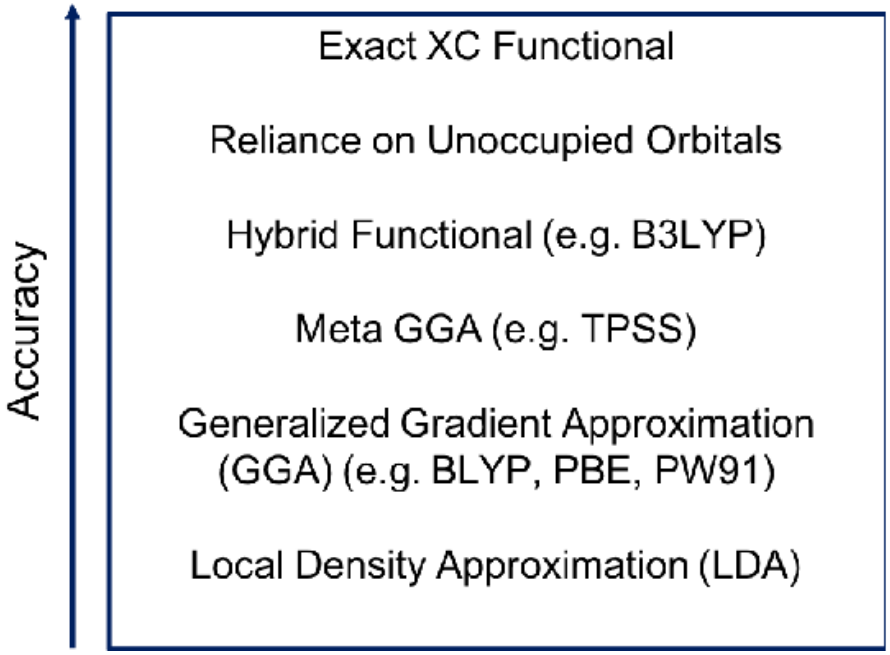

Figure 1.6: Exchange-correlation functional in the order of accuracy.

1.4.2 DFT calculations for geometry optimization

Bulk materials

Structure determines properties. Therefore, geometry optimization is always the first step of any research. To simulate geometry of a material one has to start from the crystal structure, i.e. face-centered cubic (FCC), body-centered cubic (BCC), Hexagonal close-packed (HCP), etc, and lattice constants. To find the optimized

lattice constant, the minimum total energy (E_{total}) of the material should be found first. Since E_{total} is a founction of the lattice constant. Figure 1.7 (a) is an example of lattice optimization of Cu. There is usually more than one lattice constant you need to optimize, so it is better to calsulate the lattice constants at the same time.

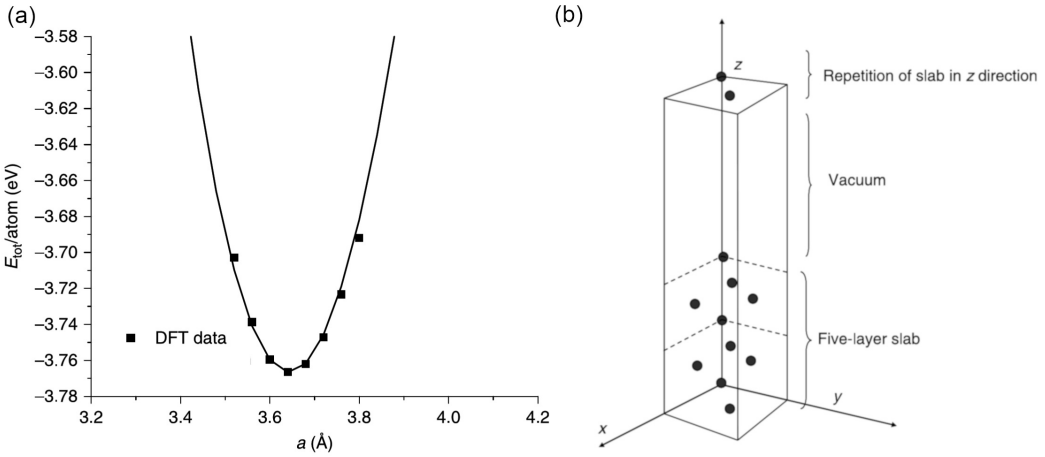

Figure 1.7: (a)Total energy, E_{total}, of Cu in the FCC crystal structure as a function of the lattice parameter, a. Data points are from DFT calculations [65]. (b) An example of slab model.

Besides, it is more convenient for DFT to calculate the structure in reciprocal space (k space). In that, there are two important DFT parameters one needs to optimize as well as lattice constant – number of k-points and cutoff energy. For more explains on the details about theory and equations about k-points and cutoff energy please check the reference [65], but basically the more the k-points and the larger the cutoff energy, the more accurate the results will be and the longer the calculation will be. So one can see there is a trade off. To figure out the enough accurate results while at the same time the the calculation take reasonable time, the number of k-points and the value of cutoff energy are needed to optimized. Again, more details are in the reference [63, 65].

Surface configurations of solids

This work focuses on surfaces, so a little bit on basis of surface simulation in DFT is discussed here. One common model scientists use to simulate surfaces is the slab model. The optimized unit cell is repeated for a number of times to make a so called supercell. Then cut the supercell for a certain direction so that a certain surface can expose. A large vacuum at the direction perpendicular to the surface should be created from last step in order to mimic the real condition, in which there is a certain amount of vacuum above surfaces. Figure 1.7 (b) is an example of surface slab model.

Density functional theory (DFT) can also simulate a lot more properties of materials such as stability, density of states, surface potentials, and magnetism etc. It is a very strong tool to analyze and predict materials.

1.5 Objectives and Scope of this Work

This work is restricted to understanding atomic structure and electronic properteis of the edges of 2D nanomaterials (i.e. WS_2 nanotube and SnS_2 nanoflakes) on the application of photoelecrochemical and electrochemical splitting. The objectives are includes:

1. To synthesize WS_2 nanotubes by two steps: synthesized WO_x nanowires by chemical vapor deposition (CVD) and sulfurization. The sulfurization conditions such as the flow rate of carrier gases and the temperatures of WO_x nanowires and S powders have to be precise so that the WO_x nanowires can be converted to WS_2 nanotubes.

2. To measure the photoelectrochemical and electrochemical performance of the WS_2 nanotubes and compare with other 2D materials such as MoS_2 nanoflakes.

3. To investigate the S arrangements and the electronic structure of the WS_2 edges with various amount of S coverages by density functional theory (DFT). This part of work should explain the good or bad PEC and/or EC performance of the WS_2 nanotubes.

4. To study the S arrangements and the electronic structure of the SnS_2 edges with various amount of S coverages by DFT. The edges of both bulk-like and monolayer SnS_2 should be done.

5. To relate the DFT results with experimental synthesis condition including temperature and pressure through thermodynamic analysis. This part should provide more details on the S arrangement of the edges of as-synthesized SnS_2 and the explanations of PEC performance of SnS_2.

Bibliography

[1] Hannah Ritchie and Max Roser. Fossil fuels. *Our World in Data*, 2020. https://ourworldindata.org/fossil-fuels.

[2] Vaclav Smil. *Energy and civilization: a history*. MIT Press, 2017.

[3] L Schlapbach, A Züttel, P Gröning, O Gröning, and P Aebi. Hydrogen for novel materials and devices. *Applied Physics A*, 72(2):245–253, 2001.

[4] Akihiko Kudo and Yugo Miseki. Heterogeneous photocatalyst materials for water splitting. *Chemical Society Reviews*, 38(1):253–278, 2009.

[5] Berit Hinnemann, Poul Georg Moses, Jacob Bonde, Kristina P Jørgensen, Jane H Nielsen, Sebastian Horch, Ib Chorkendorff, and Jens K Nørskov. Biomimetic hydrogen evolution: Mos2 nanoparticles as catalyst for hydrogen evolution. *Journal of the American Chemical Society*, 127(15):5308–5309, 2005.

[6] BE Conway and BV Tilak. Interfacial processes involving electrocatalytic evolution and oxidation of h2, and the role of chemisorbed h. *Electrochimica Acta*, 47(22-23):3571–3594, 2002.

[7] Carlos G Morales-Guio, Lucas-Alexandre Stern, and Xile Hu. Nanostructured hydrotreating catalysts for electrochemical hydrogen evolution. *Chemical Society Reviews*, 43(18):6555–6569, 2014.

[8] Stephen Fletcher. Tafel slopes from first principles. *Journal of Solid State Electrochemistry*, 13(4):537–549, 2009.

[9] JO'M Bockris and EC Potter. The mechanism of the cathodic hydrogen evolution reaction. *Journal of The Electrochemical Society*, 99(4):169–186, 1952.

[10] Akira Fujishima and K Honda. Photolysis-decomposition of water at the surface of an irradiated semiconductor. *Nature*, 238(5385):37–38, 1972.

[11] Xunyu Yang, Abraham Wolcott, Gongming Wang, Alissa Sobo, Robert Carl Fitzmorris, Fang Qian, Jin Z Zhang, and Yat Li. Nitrogen-doped zno nanowire arrays for photoelectrochemical water splitting. *Nano letters*, 9(6):2331–2336, 2009.

[12] Kazuhiko Maeda, Tsuyoshi Takata, Michikazu Hara, Nobuo Saito, Yasunobu Inoue, Hisayoshi Kobayashi, and Kazunari Domen. Gan: Zno solid solution as a photocatalyst for visible-light-driven overall water splitting. *Journal of the American Chemical Society*, 127(23):8286–8287, 2005.

[13] Kevin Sivula, Radek Zboril, Florian Le Formal, Rosa Robert, Anke Weidenkaff, Jiri Tucek, Jiri Frydrych, and Michael Gratzel. Photoelectrochemical water splitting with mesoporous hematite prepared by a solution-based colloidal approach. *Journal of the American Chemical Society*, 132(21):7436–7444, 2010.

[14] Gary Hodes, David Cahen, and Joost Manassen. Tungsten trioxide as a photoanode for a photoelectrochemical cell (pec). *Nature*, 260(5549):312–313, 1976.

[15] Lite Zhou, Chenqi Zhao, Binod Giri, Patrick Allen, Xiaowei Xu, Hrushikesh Joshi, Yangyang Fan, Lyubov V Titova, and Pratap M Rao. High light absorption and charge separation efficiency at low applied voltage from sb-doped sno2/bivo4 core/shell nanorod-array photoanodes. *Nano letters*, 16(6):3463–3474, 2016.

[16] Hongjian Yan, Jinhui Yang, Guijun Ma, Guopeng Wu, Xu Zong, Zhibin Lei, Jingying Shi, and Can Li. Visible-light-driven hydrogen production with ex-

tremely high quantum efficiency on pt–pds/cds photocatalyst. *Journal of Catalysis*, 266(2):165–168, 2009.

[17] Binod Giri, Maryam Masroor, Tao Yan, Kateryna Kushnir, Alexander D Carl, Curtis Doiron, Haochuan Zhang, Yanyan Zhao, Arthur McClelland, Geoffrey A Tompsett, et al. Balancing light absorption and charge transport in vertical sns2 nanoflake photoanodes with stepped layers and large intrinsic mobility. *Advanced Energy Materials*, 9(31):1901236, 2019.

[18] Naoki Arai, Nobuo Saito, Hiroshi Nishiyama, Kazunari Domen, Hisayoshi Kobayashi, Kazunori Sato, and Yasunobu Inoue. Effects of divalent metal ion (mg2+, zn2+ and be2+) doping on photocatalytic activity of ruthenium oxide-loaded gallium nitride for water splitting. *Catalysis Today*, 129(3-4):407–413, 2007.

[19] Shaowen Cao and Jiaguo Yu. g-c3n4-based photocatalysts for hydrogen generation. *The journal of physical chemistry letters*, 5(12):2101–2107, 2014.

[20] Savio JA Moniz, Stephen A Shevlin, David James Martin, Zheng-Xiao Guo, and Junwang Tang. Visible-light driven heterojunction photocatalysts for water splitting–a critical review. *Energy & Environmental Science*, 8(3):731–759, 2015.

[21] Zhaosheng Li, Wenjun Luo, Minglong Zhang, Jianyong Feng, and Zhigang Zou. Photoelectrochemical cells for solar hydrogen production: current state of promising photoelectrodes, methods to improve their properties, and outlook. *Energy & Environmental Science*, 6(2):347–370, 2013.

[22] Arthur J Frank, Nikos Kopidakis, and Jao Van De Lagemaat. Electrons in nanostructured tio2 solar cells: transport, recombination and photovoltaic properties. *Coordination Chemistry Reviews*, 248(13-14):1165–1179, 2004.

[23] Gopal K Mor, Karthik Shankar, Maggie Paulose, Oomman K Varghese, and Craig A Grimes. Enhanced photocleavage of water using titania nanotube arrays. *Nano letters*, 5(1):191–195, 2005.

[24] Xinjian Feng, Karthik Shankar, Oomman K Varghese, Maggie Paulose, Thomas J Latempa, and Craig A Grimes. Vertically aligned single crystal tio2 nanowire arrays grown directly on transparent conducting oxide coated glass: synthesis details and applications. *Nano letters*, 8(11):3781–3786, 2008.

[25] Yun Jeong Hwang, Akram Boukai, and Peidong Yang. High density n-si/n-tio2 core/shell nanowire arrays with enhanced photoactivity. *Nano letters*, 9(1):410–415, 2009.

[26] Kazuhiro Sayama and Hironori Arakawa. Significant effect of carbonate addition on stoichiometric photodecomposition of liquid water into hydrogen and oxygen from platinum–titanium (iv) oxide suspension. *Journal of the Chemical Society, Chemical Communications*, (2):150–152, 1992.

[27] Hironori Arakawa and Kazuhiro Sayama. Solar hydrogen production. significant effect of na 2 co 3 addition on water splitting using simple oxide semiconductor photocatalysts. *Catalysis surveys from Japan*, 4(1):75–80, 2000.

[28] Erzsébet Szabó-Bárdos, Hajnalka Czili, and Attila Horváth. Photocatalytic oxidation of oxalic acid enhanced by silver deposition on a tio2 surface. *Journal of Photochemistry and Photobiology A: Chemistry*, 154(2-3):195–201, 2003.

[29] I-Hsiang Tseng, Jeffrey CS Wu, and Hsin-Ying Chou. Effects of sol–gel procedures on the photocatalysis of cu/tio2 in co2 photoreduction. *Journal of Catalysis*, 221(2):432–440, 2004.

[30] Soonhyun Kim and Wonyong Choi. Dual photocatalytic pathways of trichloroacetate degradation on tio2: effects of nanosized platinum deposits on kinetics and mechanism. *The Journal of Physical Chemistry B*, 106(51):13311–13317, 2002.

[31] Wonyong Choi, Andreas Termin, and Michael R Hoffmann. The role of metal ion dopants in quantum-sized tio2: correlation between photoreactivity and charge carrier recombination dynamics. *The Journal of Physical Chemistry*, 98(51):13669–13679, 2002.

[32] K Gurunathan, P Maruthamuthu, and MVC Sastri. Photocatalytic hydrogen production by dye-sensitized pt/sno2 and pt/sno2/ruo2 in aqueous methyl viologen solution. *International Journal of Hydrogen Energy*, 22(1):57–62, 1997.

[33] Ryu Abe, Kazuhiro Sayama, and Hironori Arakawa. Efficient hydrogen evolution from aqueous mixture of i- and acetonitrile using a merocyanine dye-sensitized pt/tio2 photocatalyst under visible light irradiation. *Chemical Physics Letters*, 362(5-6):441–444, 2002.

[34] Andreas Kay, Ilkay Cesar, and Michael Grätzel. New benchmark for water photooxidation by nanostructured α-fe2o3 films. *Journal of the American Chemical Society*, 128(49):15714–15721, 2006.

[35] Jeremie Brillet, Michael Gratzel, and Kevin Sivula. Decoupling feature size and functionality in solution-processed, porous hematite electrodes for solar water splitting. *Nano letters*, 10(10):4155–4160, 2010.

[36] Niclas Beermann, Lionel Vayssieres, Sten-Eric Lindquist, and Anders Hagfeldt. Photoelectrochemical studies of oriented nanorod thin films of hematite. *Journal of the Electrochemical Society*, 147(7):2456–2461, 2000.

[37] Guanjie Ai, Hongxing Li, Shaopei Liu, Rong Mo, and Jianxin Zhong. Solar water splitting by tio2/cds/co–pi nanowire array photoanode enhanced with co–pi as hole transfer relay and cds as light absorber. *Advanced Functional Materials*, 25(35):5706–5713, 2015.

[38] Jingshan Luo, Lin Ma, Tingchao He, Chin Fan Ng, Shijie Wang, Handong Sun, and Hong Jin Fan. Tio2/(cds, cdse, cdses) nanorod heterostructures and photoelectrochemical properties. *The Journal of Physical Chemistry C*, 116(22):11956–11963, 2012.

[39] Chen-Zhong Yao, Bo-Hui Wei, Li-Xin Meng, Hui Li, Qiao-Juan Gong, Hong Sun, Hui-Xuan Ma, and Xiao-Hua Hu. Controllable electrochemical synthesis and photovoltaic performance of zno/cds core–shell nanorod arrays on fluorine-doped tin oxide. *Journal of Power Sources*, 207:222–228, 2012.

[40] Quanjun Xiang, Jiaguo Yu, and Mietek Jaroniec. Preparation and enhanced visible-light photocatalytic h2-production activity of graphene/c3n4 composites. *The Journal of Physical Chemistry C*, 115(15):7355–7363, 2011.

[41] Yang Hou, Fan Zuo, Alexander P Dagg, Jikai Liu, and Pingyun Feng. Branched wo3 nanosheet array with layered c3n4 heterojunctions and coox nanoparticles as a flexible photoanode for efficient photoelectrochemical water oxidation. *Advanced materials*, 26(29):5043–5049, 2014.

[42] Junya Sato, Nobuo Saito, Yoko Yamada, Kazuhiko Maeda, Tsuyoshi Takata, Junko N Kondo, Michikazu Hara, Hisayoshi Kobayashi, Kazunari Domen, and

Yasunobu Inoue. Ruo2-loaded β-ge3n4 as a non-oxide photocatalyst for overall water splitting. *Journal of the American Chemical Society*, 127(12):4150–4151, 2005.

[43] Kazuhiko Maeda, Nobuo Saito, Daling Lu, Yasunobu Inoue, and Kazunari Domen. Photocatalytic properties of ruo2-loaded β-ge3n4 for overall water splitting. *The Journal of Physical Chemistry C*, 111(12):4749–4755, 2007.

[44] MG Kibria, S Zhao, FA Chowdhury, Q Wang, HPT Nguyen, ML Trudeau, H Guo, and Z Mi. Tuning the surface fermi level on p-type gallium nitride nanowires for efficient overall water splitting. *Nature communications*, 5(1):1–6, 2014.

[45] Yu-Xiang Yu, Wei-Xin Ouyang, Zhou-Ting Liao, Bin-Bin Du, and Wei-De Zhang. Construction of zno/zns/cds/cuins2 core–shell nanowire arrays via ion exchange: p–n junction photoanode with enhanced photoelectrochemical activity under visible light. *ACS applied materials & interfaces*, 6(11):8467–8474, 2014.

[46] Yongfu Sun, Zhihu Sun, Shan Gao, Hao Cheng, Qinghua Liu, Junyu Piao, Tao Yao, Changzheng Wu, Shuanglin Hu, Shiqiang Wei, et al. Fabrication of flexible and freestanding zinc chalcogenide single layers. *Nature communications*, 3(1):1–7, 2012.

[47] Jinzhan Su, Xinjian Feng, Jennifer D Sloppy, Liejin Guo, and Craig A Grimes. Vertically aligned wo3 nanowire arrays grown directly on transparent conducting oxide coated glass: synthesis and photoelectrochemical properties. *Nano letters*, 11(1):203–208, 2011.

[48] Changgu Lee, Xiaoding Wei, Jeffrey W Kysar, and James Hone. Measurement of the elastic properties and intrinsic strength of monolayer graphene. *science*, 321(5887):385–388, 2008.

[49] Guangbo Liu, Zhonghua Li, Tawfique Hasan, Xiaoshuang Chen, Wei Zheng, Wei Feng, Dechang Jia, Yu Zhou, and PingAn Hu. Vertically aligned two-dimensional sns 2 nanosheets with a strong photon capturing capability for efficient photoelectrochemical water splitting. *Journal of Materials Chemistry A*, 5(5):1989–1995, 2017.

[50] Branimir Radisavljevic, Aleksandra Radenovic, Jacopo Brivio, Valentina Giacometti, and Andras Kis. Single-layer mos 2 transistors. *Nature nanotechnology*, 6(3):147, 2011.

[51] Zongyou Yin, Hai Li, Hong Li, Lin Jiang, Yumeng Shi, Yinghui Sun, Gang Lu, Qing Zhang, Xiaodong Chen, and Hua Zhang. Single-layer mos2 phototransistors. *ACS nano*, 6(1):74–80, 2012.

[52] Maurizia Palummo, Marco Bernardi, and Jeffrey C Grossman. Exciton radiative lifetimes in two-dimensional transition metal dichalcogenides. *Nano letters*, 15(5):2794–2800, 2015.

[53] Nardeep Kumar, Jiaqi He, Dawei He, Yongsheng Wang, and Hui Zhao. Charge carrier dynamics in bulk mos2 crystal studied by transient absorption microscopy. *Journal of Applied Physics*, 113(13):133702, 2013.

[54] Xudong Wang, Peng Wang, Jianlu Wang, Weida Hu, Xiaohao Zhou, Nan Guo, Hai Huang, Shuo Sun, Hong Shen, Tie Lin, et al. Ultrasensitive and broadband mos2 photodetector driven by ferroelectrics. *Advanced materials*, 27(42):6575–6581, 2015.

[55] Guoxiong Su, Viktor G Hadjiev, Phillip E Loya, Jing Zhang, Sidong Lei, Surendra Maharjan, Pei Dong, Pulickel M. Ajayan, Jun Lou, and Haibing Peng. Chemical vapor deposition of thin crystals of layered semiconductor sns2 for fast photodetection application. *Nano letters*, 15(1):506–513, 2015.

[56] Yunzhou Xue, Yupeng Zhang, Yan Liu, Hongtao Liu, Jingchao Song, Joice Sophia, Jingying Liu, Zaiquan Xu, Qingyang Xu, Ziyu Wang, et al. Scalable production of a few-layer mos2/ws2 vertical heterojunction array and its application for photodetectors. *Acs Nano*, 10(1):573–580, 2016.

[57] Thomas F Jaramillo, Kristina P Jørgensen, Jacob Bonde, Jane H Nielsen, Sebastian Horch, and Ib Chorkendorff. Identification of active edge sites for electrochemical h2 evolution from mos2 nanocatalysts. *science*, 317(5834):100–102, 2007.

[58] Tzu-Yin Chen, Yung-Huang Chang, Chang-Lung Hsu, Kung-Hwa Wei, Chia-Ying Chiang, and Lain-Jong Li. Comparative study on mos2 and ws2 for electrocatalytic water splitting. *International journal of hydrogen energy*, 38(28):12302–12309, 2013.

[59] HS Song, SL Li, L Gao, Y Xu, K Ueno, J Tang, YB Cheng, and K Tsukagoshi. High-performance top-gated monolayer sns 2 field-effect transistors and their integrated logic circuits. *Nanoscale*, 5(20):9666–9670, 2013.

[60] Yang Cui, Run Xin, Zhihao Yu, Yiming Pan, Zhun-Yong Ong, Xiaoxu Wei, Junzhuan Wang, Haiyan Nan, Zhenhua Ni, Yun Wu, et al. High-performance monolayer ws2 field-effect transistors on high-κ dielectrics. *Advanced Materials*, 27(35):5230–5234, 2015.

[61] Robert G Parr. Density functional theory of atoms and molecules. In *Horizons of Quantum Chemistry*, pages 5–15. Springer, 1980.

[62] Kieron Burke. Perspective on density functional theory. *The Journal of chemical physics*, 136(15):150901, 2012.

[63] Paul Geerlings, F De Proft, and W Langenaeker. Conceptual density functional theory. *Chemical reviews*, 103(5):1793–1874, 2003.

[64] Pierre Hohenberg and Walter Kohn. Inhomogeneous electron gas. *Physical review*, 136(3B):B864, 1964.

[65] David Sholl and Janice A Steckel. *Density functional theory: a practical introduction*. John Wiley & Sons, 2011.

Chapter 2

Edge-on Oriented Tungsten Disulfide (WS_2) Nanotubes

2.1 Introduction

Tungsten disulfide (WS_2) and related transition metal dichalcogenides (TMDs) has drawn lots of interests for solar energy conversion and electrocatalysis because of their layered structure and resulting unique optoelectronic and chemical properties. Besides, the orientation of WS_2 layers and the electronic structure of the edges has a large influence on its performance. WS_2 crystals, the same as other 2D materials, consist of layers held together by weak van der Waals forces. Therefore, there is fast charge transport within the layers but very slow transport across the layers, which leads us to this project. Due to the similarity of crystal structure to MoS_2 and proper band gap energy, WS_2 is hypothesized to be a good electrocatalyst for water splitting. The edge-on oriented WS_2 nanotubes was studied through experiments and simulation in this chapter, including a comparison with MoS_2 nanoflakes synthesized by chemical vapor deposition (CVD).

2.2 Experimental and Computational Methods

2.2.1 Synthesis of WS_2 nanotubes

WO_x nanowire growth

WO_x nanowires were grown by chemical vapor deposition (CVD) method in a three-zone tube furnace. The tube furnace was connected to a vacuum pump that created a pressure of 60 - 140 mTorr. A small flow rate of N_2 as a carrier gas was connected at the other end of the tube furnace. The WO_3 powder was set at the upstream side at the temperature of 900 °C. The substrates were set at the downstream side at the temperature around 650 °C. Before starting to heat up the furnace, the vacuum pump and N_2 flow were turned on for around 20 min to purge the tube. After that, the furnace was set to heat up to the target temperatures within 1 hour, and was then maintained at the target temperatures for 30 min for the growth of the nanowires. The samples were allowed to cool down inside the furnace until at room temperature.

WO_x seed layer coating

The nanowires did not easily nucleate directly on the Si and SiO_2/Si wafers, because the smooth surface of the Si wafers lacks nucleation sites. 15 and 50 nm thick W were deposited on SiO_2/Si wafers using magnetron sputter in Harvard University. Therefore, WO_x nano-particles were spin coated as a seed layer on these substrates before nanowire growth. The solution of seed layer was a mixture of 1.25 g H_2WO_4, 0.5 g polyvinyl alcohol (PVA) and 18 mL of 30 w% H_2O_2. The solution was stirred overnight before use. The solution was then spin coated onto the substrates at 2000 rpm for 30 s followed by hotplate annealing at 500 °C for 10 to 15 min for each layer.

Sulfurization of WO_x to WS_2

The WO_x nanowires were sulfurized to convert them to WS_2 in the same three-zone tube furnace. The substrates with WO_x nanowires were set at the downstream side at the temperature of 820 °C [1, 2]. The sulfur powders were set at the upstream side at the temperature of 200 °C. At the end of downstream side of the furnace, a saturated NaOH solution was connected to the tube furnace to absorb remaining sulfur gas. N_2 flow was turned on first to check leakage and purge the whole setup before turning on the furnace. Then carrier gases, which are 100 sccm N_2 and 5 sccm H_2, were flowed through the tubecfurnace. When the temperature reached the target value (in 60 min), the temperature was maintained for another 1.5 hours. The samples were then allowed to cool down inside the furnace until at room temperature.

Substrate transfer

Transfer of the WS_2 layer from SiO_2/Si substrates to indium tin oxide (ITO) coated glass substrates was also attempted to enable PEC measurement, because ITO glass is transparent and conductive, which are both needed for PEC measurements, but is not able to tolerate the synthesis and sulfurization temperatures. The transfer procedure is shown in Figure 2.1 (a). First, a layer of poly(methyl methacrylate) (PMMA) is spin coated to protect the WS_2 from contamination and damage in the following steps. When the PMMA layer was dry, the entire sample was soaked into 1M KOH solution at 360K until the PMMA/WS_2 completely detached from substrate. This occurs because KOH solution dissolves SiO_2 and therefore the PMMA/WS_2 layer can separate from the SiO_2/Si substrate. The SiO_2/Si substrate was then removed and the PMMA/WS_2 layer was carefully transferred to a DI water bath. ITO glass substrate was then used to fish out the PMMA/WS_2 layer from DI water followed by washing away the PMMA layer with acetone, leaving behind the transferred WS_2

layer on the ITO substrate.

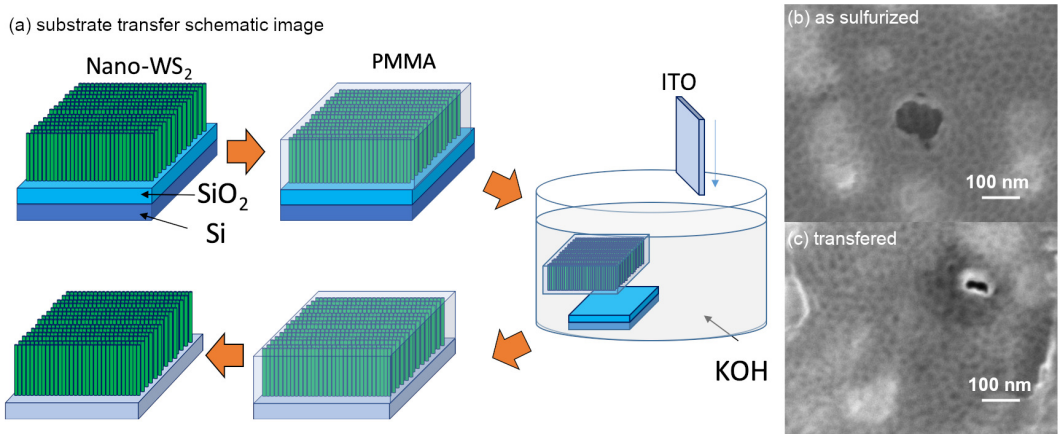

Figure 2.1: (a) schematic images of substrate transfer. The resin procudure with DI water was not showed here. (b) SEM image of the WS_2 nano-porous film on SiO_2/Si substrate; and (c) SEM image of the WS_2 nano-porous film after transfer to ITO glass substrate.

2.2.2 Synthesis of MoS_2 nanoflakes

MoS_2 nanoflakes were grown by CVD in a one-zone tube furnace. The S powder was placed outside the furnace with an external heat source at the upstream side. 120 mg of molybdenum oxide (MoO_3) powder was set at downstream side with a Mo foil substrate laying horizontally above. The tube furnace was purged by 500 sccm Ar gas for 10 min after setup was done. Then the S powder and MoO_3 were heated up from room temperature to 200 °C and 850 °C, respectively, in 40 min and were held at those temperatures for another 40 min. After the growth procedure, the whole setup was allowed to cool down to room temperature naturally inside the furnace.

2.2.3 Measurements and characterization

PEC and EC measurements

PEC and EC measurements of MoS_2 and WS_2 were done with a three-electrode configuration. Electrolyte is 0.5M H_2SO_4. The counter electrode was Pt wire and the reference electrode was a saturated calomel electrode (SCE). All voltages were converted to reversible hydrogen electrode (RHE) by

$$V_{RHE} = V_{SCE} + 0.059 \times pH + 0.244. \tag{2.1}$$

The WS_2 and MoS_2 electrodes were made by sticking nickel-chromium alloy wire to the substrates using silver epoxy (Ted Pella #16043), followed by nonconductive epoxy (Loctite 1C) covering the silver epoxy and the whole back area of the electrodes.

A xenon lamp (model 6258, Oriel) equipped with an AM1.5G gilter (model 81094, Oriel) provided the simulated sunlight for all PEC measurements.

Structural Characterization

The morphologies of nanostructures of WS_2 and MoS_2 were characterized using scanning electron microscopy (SEM) (JEOL 7000F, 10 kV), and parallel beam x-ray diffraction (XRD) (PANalytical Empryrean, Cu kα, 45 kV, 40 mA).

The grain sizes of WS_2 nanotubes were estimated by Sherrer Equation:

$$\tau = \frac{K\lambda}{\beta \cos\theta}. \tag{2.2}$$

Where K is Sherrer constant which is 0.86 in this case; λ is the wavelength of Cu-kα X-ray which is 0.154056 nm; β is the line broadening at half the maximum intensity

(FWHM) at θ angle; and θ is the Bragg angle of the peak.

2.2.4 Computational Details

All of the simulations were utilized with the Vienna ab initio simulation package (VASP) [3, 4, 5, 6]. The convergence criteria of the electronic and ionic relaxations were 10^{-5} eV and 0.01 eV/Å, respectively. A plane wave cutoff energy of 400 eV was used. A 6x6x2 Gamma centered k-point grid was used for lattice optimization of bulk WS_2. A single k-point was used for slab models because of the large size of the super cells described below. For density of states simulation for bulk WS_2 a significant larger k-point grid 10x10x2 was used. The generalized gradient approximation (GGA) with the Perdew-Burke-Ernzerhof (PBE) [7] exchange correlation functional was used for all geometry optimizations and density of states (DOS) simulation. The Grimme's zero damping DFT-D3 method [8, 9] was used in all calculations to describe the van der Waals interaction between the layers of WS_2.

Figure 2.2 shows the slab model for geometry simulation of WS_2 edges. The slab models were made with extension of optimized WS_2 unit cell with $(10\bar{1}0)$ surface/edge exposing. There was around 18 Åvacuum in the z-direction, so that the edges behave like surface. Each supercell contains two vertical S-W-S sandwich layer where each vertical layer consists of 6W layers for geometry simulation. Each vertical layer of WS_2 had two edges – S terminated edges (S edges) and W terminated edges (W edges). Here we modeled the sulfur arrangement and DOS of both edges. Figure 2.2 shows 100% sulfur covered S-edge and 0% sulfur covered W edge. Besides, in order to calculate DOS more accurately, meaning to make DOS of the middle two layers have bulk-like shape, 8W-layer slabs with the optimized geometry from 6W-layer slabs were used.

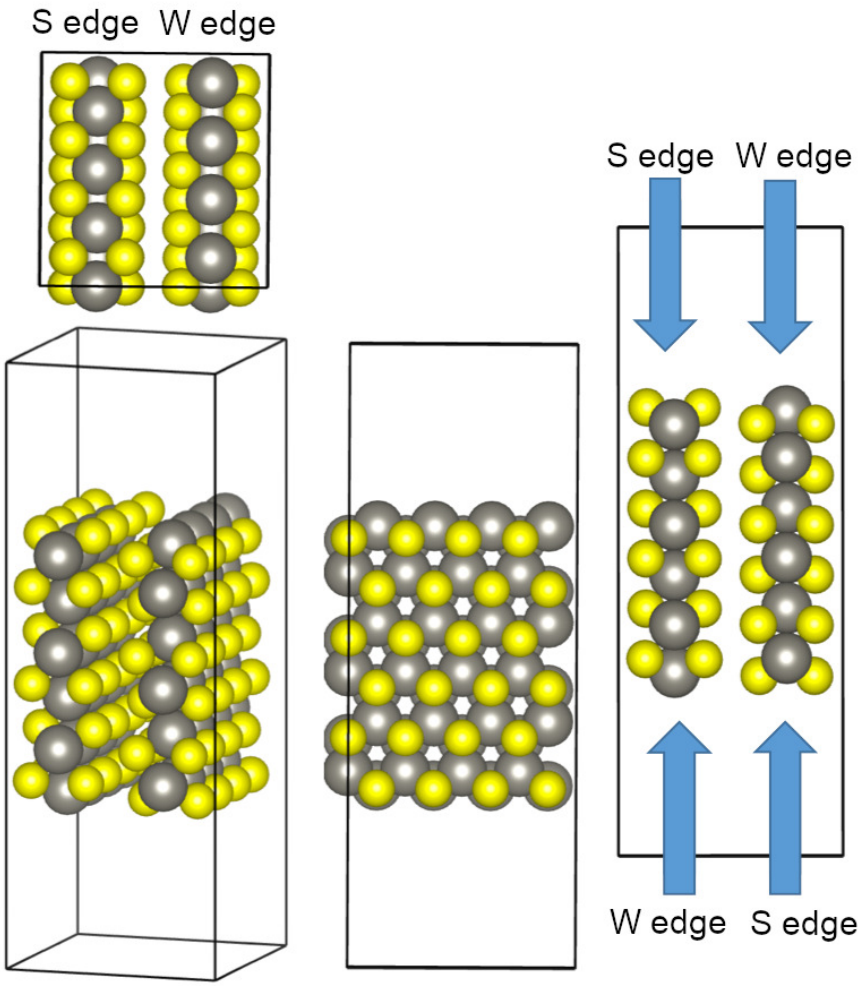

Figure 2.2: Slab model for WS_2 edge simulation. Yellow balls represent S atoms and grey balls are W atoms.

2.3 Results and Discussion

2.3.1 Morphology

WO_x nanowires were attempted to synthesized on multiple substrates including Ti foil, W foil, and Si wafer. Figure 2.3 shows SEM and XRD of the nano-wires. Ti foil was not ideal at all among all these substrates, because there is no growth observed on the surface even when seed layers were coated prior to the growth. The synthesis

on Si wafers are better when seed layers were coated on top of the sputtered W layer. When the sputtered W layer was thicker, the WO_x nanowires tend to grow longer (Figure 2.3(d) and (e)). This could because the source of WO_x nanowires was not 100% come from WO_3 powder, the W on the substrate surface also involved in the growth. Another evidence for this hypothesis is the composition of the nanowires was not WO_2, but $WO_{2.72}$ ($W_{18}O_{49}$) according XRD results. Hence, since 15 nm thick W layer had fewer W atoms than 50 nm one does, so there was less W source for WO_x nanowires grow, leading to shorter nanowires. W foil was the best since WO_x nanowires was able to grow perfectly even without seed layers. From SEM images of WO_x nanowires on both W and Si wafer (Figure 2.3 (a) and (e)), one can see that good nanowires are around 450 to 600 nm long. Besides, from figure 2.3 (a) to (c) one can see that the WO_x nanowires tended to grow longer at higher vacuum condition. This suggests that vacuum could affect the growth rate of WO_x nanowires and the lower the pressure was, the longer the WO_x nanowires would be, which makes sense, because there were less resistance for nanowires growth at higher vacuum condition.

Although the tungsten oxide source powder is initially WO_3, XRD patterns in Figure 2.3 (f) show that the WO_x nanowires are composed of $W_{18}O_{49}$ ($WO_{2.72}$), not WO_3. It was also observed that high vacuum and high purity of carrier gas is very critical for the synthesis of the nanowires, and that the source powders become a dard color (indicative of reduction, likely to $W_{18}O_{49}$) during the synthesis. Since the evaporation of $W_{18}O_{49}$ is easier than that of WO_3, having low oxygen concentration in the tube is critical for the generation of sufficient vapor concentration for the growth of the nanowires. If the pressure was too high or the carrier gas (N_2 in this case) contained large concentration of O_2, the WO_3 source powder would not be reduce, and insufficient vapor would be generated, leading to a failure of nanowire

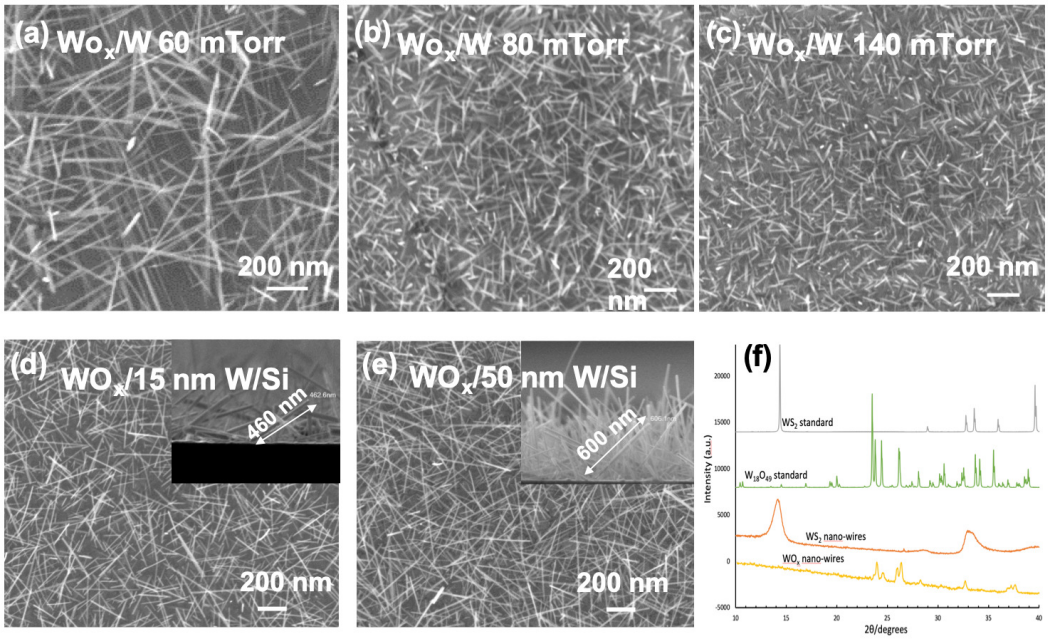

Figure 2.3: SEM images of WO_x nanowires grown on W foil at 60 mTorr (a), 80 mTorr (b), and 140 mTorr (c); SEM images of WO_x nanowires grwon on Si wafer with 15 nm thick W coating layer (d), and 50 nm thick W coating layer (e); XRD pattern of WO_x nanowires and WS_2 nanotubes.

synthesis. The broad peak of the WS_2 suggests that the nanotubes were consist of small size WS2 grains. In fact, the grain size of the WS2 were estimated by Scherrer Equation is from 7.5 to 8.5 nm. Comparing with the 10-20 nm of the diameter of the nanotubes observed in SEM, one can determine that there were many small WS2 grains within each nanotubes.

To completely sulfurize WO_x nanowires to WS_2 nanotubes, high accurate experimental condition was required. The H_2 had to account for 5% of total carrier gas and the temperature of WO_x nanowires had to be at 820 °C. Only under this condition, can one covert WO_x nanowires to WS_2 nanotubes with multilayered structure [1]. Figure 2.4 (a) shows the WS_2 nanotubes coverted from WO_x nanowires on W foil substrate preserving original wire shape. The structure of multilayered nanotubes is critical because it provides edge-on orientation. However, the edges of the WS_2

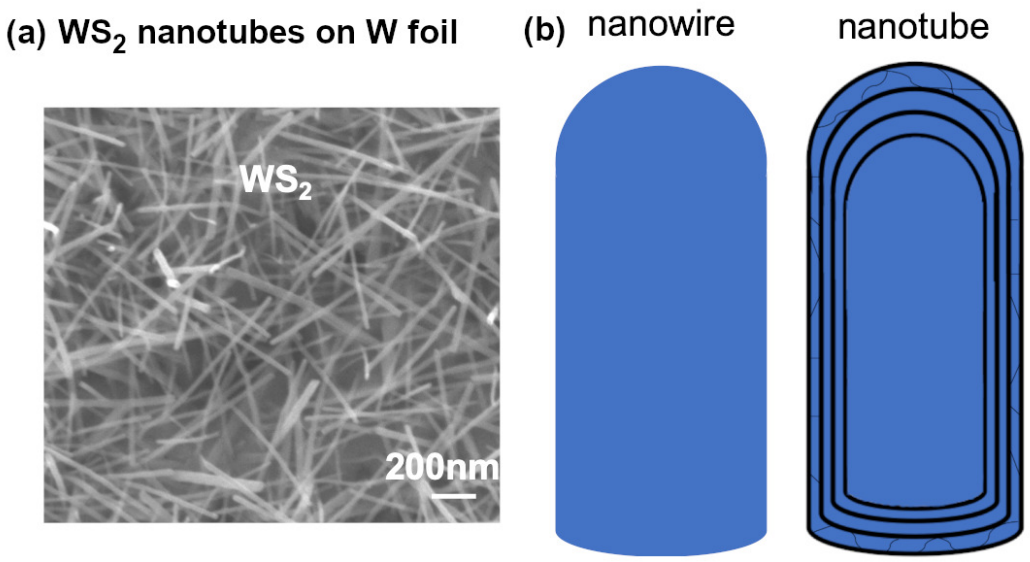

Figure 2.4: SEM image of WS_2 nantubes on W foil (a), and a schematic diagram of a nanowire and a cross section of a nanotube (b).

nanotubes were not exposed, which explains the relative bad EC performance. Figure 2.4 (b) is a schematic diagram of the structure of a WO_x nanowaire and a WS_2 multilayered nanotube.

One of typical charge collector of WS_2 is indium tin oxide (ITO) glass. Since the synthesis condition was too harsh for ITO glass to survive, the WS_2 nanotubes were transferred to ITO after synthesizing on other substrates. To do that, the growth of WS_2 nanotubes on SiO_2 coated Si wafer (SiO_2/Si) followed by transferring to ITO glass was done. However the transfer of the nanotubes was a bit challenging and the successful rate was quite low, since the nanotubes could be easily destroyed or pushed down during the transfer. WO_x nanoporous thin film was synthesized and provided by the laboratory of Prof. Stefik in University of South Carolina. So the WO_x nanofilms were sulfurized with the same methods and transferred the film to ITO glass (see Figure 2.1). Figure 2.1 (b) and (c) shows the nanoporous film before and after substrate transfer. One can tell that the transfer methods worked well on

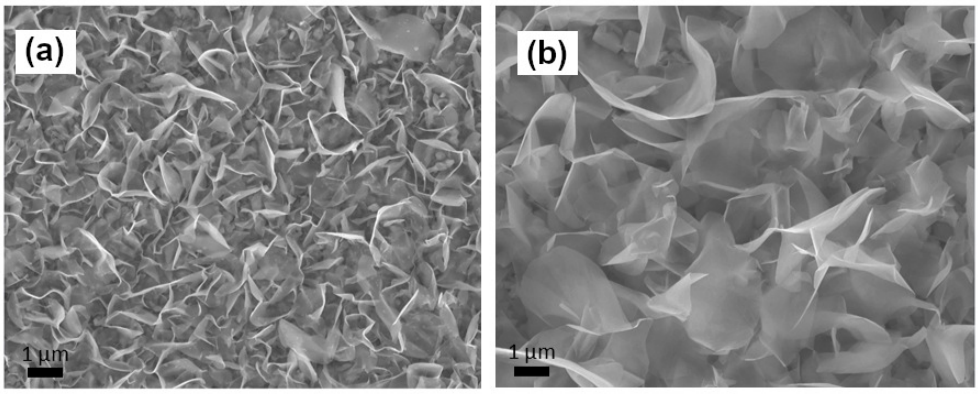

Figure 2.5: SEM images of MoS_2 nanoflakes.

the thin film in terms of preserving the nanostructure of WS_2 well.

In order to compare performance of WS_2 nanotubes with MoS_2, MoS_2 vertical nanoflakes were synthesized by CVD. This part of work was done by Jeremy Jacobs. The edge-on orientated MoS_2 were synthesized by CVD directly, but the morphology of MoS_2 was more likely to form vertical nanoflakes. Figure 2.5 shows SEM images of the MoS_2 nanoflakes. One can see from the SEM images that the MoS_2 nanoflakes were very thin and also the packing density was quite high, which provides numerous edges, i.e. numerous reactive sites.

2.3.2 PEC performance

Since the synthesis of edge-on oriented WS_2 was achieved, an impressive photo-electrochatalysis performance from it was expected. However, similar to MoS_2 nanoflakes WS_2 nanotubes as well as the transferred nanoporous thin films did not have any photoresponse. Figure 2.6 (a) shows PEC and EC measurements for MoS_2 nanoflakes and WS_2 nanotubes. One can see that for MoS_2 nanoflakes, the curves with and without light shining are almost the same, and the curve with chopped light does not show photo-response. The curve for WS_2 nanotubes with chopped

light does not show any photo-response either. This phenomenon is interesting because the edge-on oriented edge-rich MoS_2 and WS_2 with band gap energies around from 1.3 to 1.5 eV were thought to be very promising for PEC applications until now.

As a typical 2D materials, MoS_2 has been studied as an elecrocatalyst in HER for decades [10, 11, 12], but there is very few reports on photoelectrocatalysis of MoS_2. When looked into the structure of these edge-rich MoS_2, it is found using STM measurement and DFT simulation that the edges of MoS_2 are surprisingly metallic [13]. This makes the charge recombination rate at the edges become very high, meaning photo-generated electrons recombine with holes so quickly that no more photo-generated electrons can involve in electrocatalysis reaction with electrolyte. More detail, one can treat the metallic edges as a series of defects which therefore provide defect states in the bandgap 2.6 (b) and (c). In other words, the metallic edges could form charge traps between valence band and conduction band of the semiconductor. Since this defects has very high density (almost 100%), the defect states/traps in the bandgap is almost continuous. So the charge recombination rate at the edges is almost 100%.

However, this is a theory that was used to explain the poor PEC performance of the metallic edges of MoS_2. At the time we did this project, there was no publication talking about the subjects of WS_2 that MoS_2 is familiar with, including structure and properties of the edges. Hence, density functional theory (DFT) simulation was done to study the edge configurations and their electronic properties in order to find the reason that the edge-on orientated WS_2 do not have photo-response.

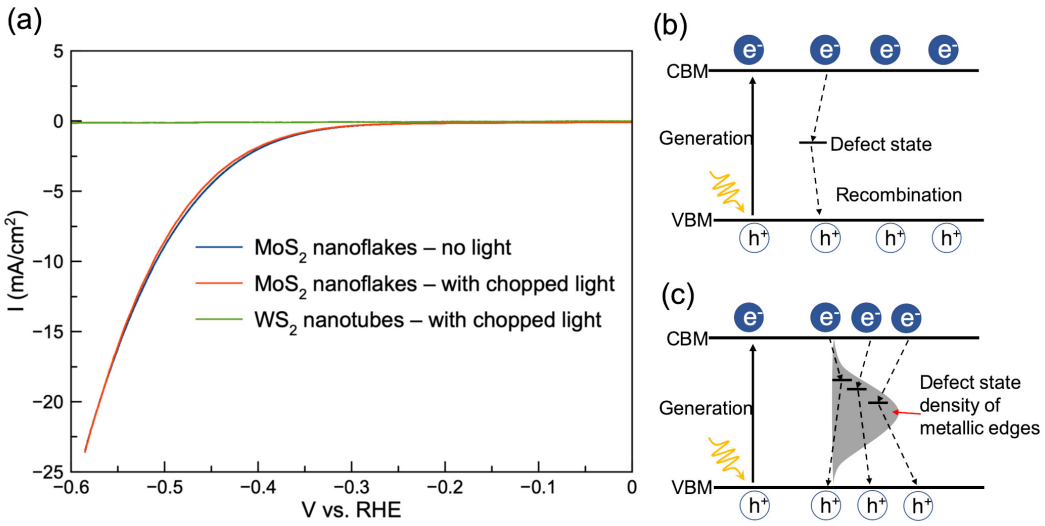

Figure 2.6: PEC and EC performance of MoS_2 nanoflakes and WS_2 nanotubes (a), photo-generated electron recombination schematic diagram for semiconductors with on defect state (b), and photo-generated electron recombination schematic diagram for semiconductors with metallic edges (c).

2.3.3 S arrangement at WS_2 edges by DFT

As mentioned above, the slab model for edge simulation was obtained by extend the optimized unit cell of WS_2. That is to say geometry optimization of bulk WS_2 was done before simulate any edges. Calculated the bulk lattice parameters as a = b = 3.16 Å, c = 12.01 Å, which agree with previous experimental values (a = b = 3.15 Å, c = 12.32 Å) [14] well. The band gap energy of bulk WS_2 should be around 1.3 eV [15, 16], however, since the PBE functional always underestimates band gap energy, the band gap energy of bulk WS_2 from our simulation was 1.0 eV which is consistent with other DFT simulation with PBE functional [17].

There are various possible arrangements of WS_2 edges with regards to S positions on both S and W edges. 0, 25, 50, 75, and 100% S coverages of both edges were simulated. Each edge adsorbed 0, 2, 4, 6, and 8 S atoms accordingly. However, there could be numerous possibilities of S arrangement for each coverage. Fortu-

Table 2.1: Adsorption energies of WS_2 edges in eV.

% of S at W edge	% of S at S edge			
	0	25	75	100
0	0	-4.22	-2.59	-2.32
25	-3.58	-3.88	-2.84	-2.55
50	-2.61	-3.06	-2.70	-2.39
75	-1.81	-2.04	-2.20	-1.96
100		-1.12		

nately, the crystal structure of WS_2 is the same as 2H-MoS_2. To avoid wasting time on unstable initial structures, so the edge configuration of WS_2 followed previous publications of 2H-MoS_2 edges Therefor,with 2H-MoS_2 as a reference [18, 19, 20], the same arrangements of 2H-MoS_2 edges at WS_2 edges were simulated and then the whole slab was allowed to relax. The top and bottom two atomic layers of the slab model were treated as edges, while the middle four atomic layers were supposed to be bulk-like. Figure 2.7 shows all of the initial edge configurations that were simulated. The yellow sphere with a cross are the S atoms at the edges. The digits represent the percentage of S at the edge and the letters represent different edges (W or S edge). For example, 25S-50W means S edge was covered by 25% of sulfur atoms and W edge was covered by 50% at the same time. The most of these initial converged without obvious changing except the ones with 50% sulfur atoms at S edge did not converge.

By calculating adsorption energy of sulfur atom, the relative stability of the edges at 0 K can be determined, because DFT simulation is based on 0 K. The adsorption reaction can be written like following:

$$0S - 0W + H_2S \rightarrow iW - jS + H_2. \tag{2.3}$$

That is to say that the adsorption energy was calculated by

$$E_{ad} = \frac{1}{n}(E_{iW-jS} - E_{0W-0S} - nE_{H_2S} + nE(H_2)), \tag{2.4}$$

where n is the total number of sulfur atoms the slab adsorbed; E_{iW-jS} is DFT total energy of iW-jS slab; i and j are the percentage of sulfur atoms at W and S edge, respectively; E_{0W-0S} is DFT total energy of 0W-0S slab; and E_{S_2} is DFT total energy of S_2 gas. Table 2.1 tabulates the adsorption energies of the converged edges. One can see from the table that the most stable edge is 0W-25S at 0K.

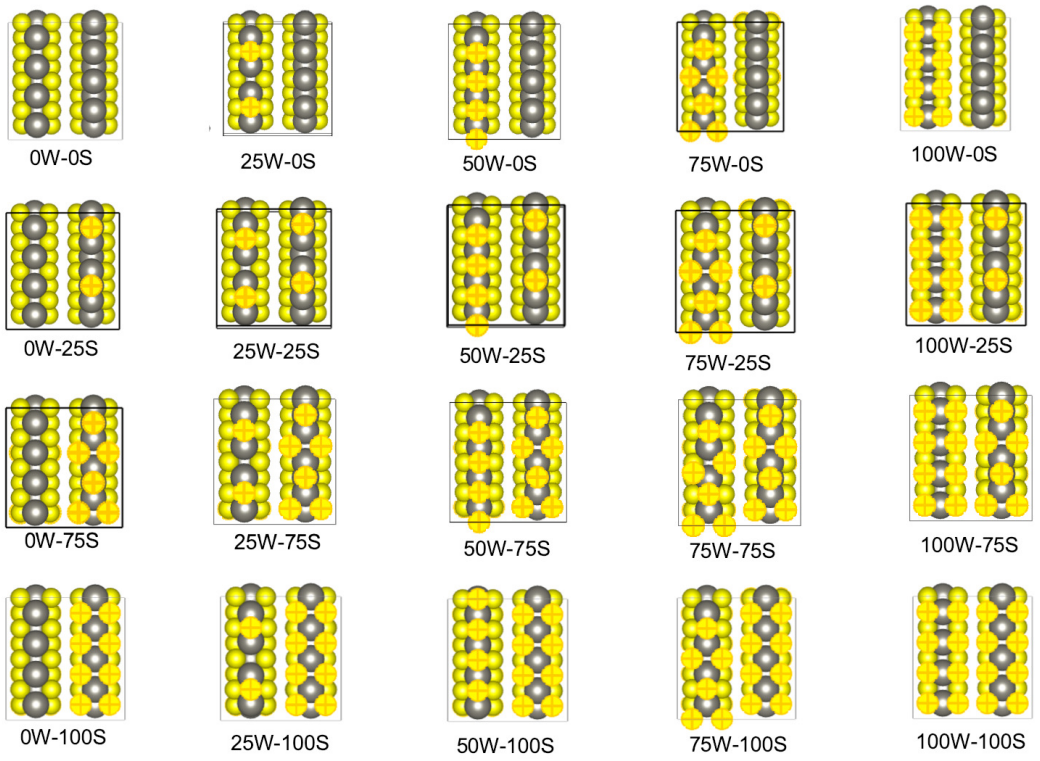

Figure 2.7: All of initial edge configurations simulated for WS_2. The digits represent the percentage of S at the edges and the letters represent different edges (W or S edge). The yellow sphere are S and the grey ones are W. The S atoms with a cross are the S atoms at the edges.

2.3.4 Density of states (DOS) of WS_2 edges

In order to check if the edges of WS_2 are the same as 2H-MoS_2, i.e., to sneak peek if the edges of WS_2 are metallic or not, several quick simulation of electronic structure by PEB exchange-correlation functional was done. Although PBE functional tends to underestimate the band gap energy, it takes shorter time and can provide a band gap energy trend in this case. The results meet our expectations that the edges of WS_2 are metallic (see Figure 2.8), just like 2H-MoS_2. The DOS of 0W-25S, the most stable one, and 50S-75S, a random one are shown here. DOS for other converged edges were also simulated, please see more DOS plots in appendix A Figure A.1. One can see from Figure 2.8 that both W- and S-edges have 0 band gap energies around Fermi energy. The middle two layers were bulk-like, therefore the DOS from the middle two layers hae band gaps shown up. Because of the PBE functional, the band gap energies of the middle two layers were much smaller than their actual value (1.3 eV). In summary, the metallic edges of WS_2 according to our DFT simulation explains why edge-on orientated WS_2 nanotubes do not response to sunlight.

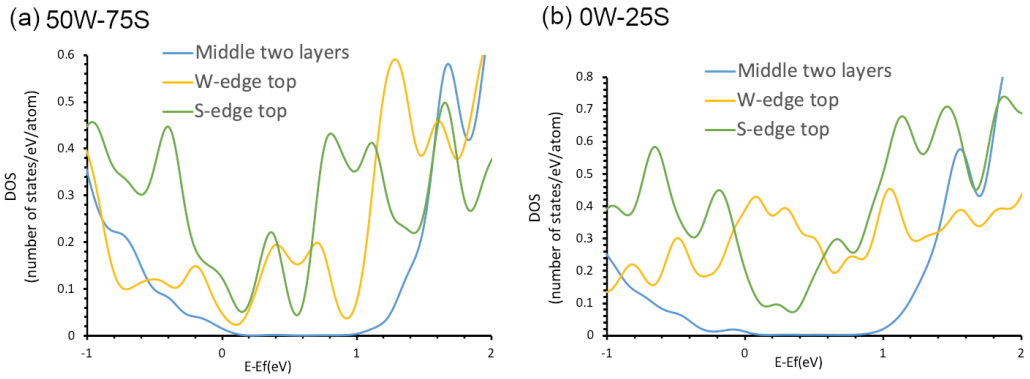

Figure 2.8: Density of states (DOS) of two 50S-75S (a) and 0S-25S (b) WS_2 slabs. The green curves represent the DOS of S edges; the orange curves represent the DOS of W edges; and the blue curves represent the DOS of middle two layers of the slab model, i.e. the bulk WS_2.

2.4 Conclusion

In this Chapter, the edge-on oriented WS_2 nanotubes and MoS_2 nanoflakes were synthesized. The photoelectrochemical (PEC) and electrochemical (EC) reactions were tested on both of the two materials. Neither the WS_2 nanotubes nor the MoS_2 nanoflakes had photoresponse, while MoS_2 nanoflakes had excellent EC performance. According to the estimation from X-ray diffraction pattern, the grain size of WS_2 nanotubes was much smaller than the diameter and the length of the nanotube, meaning each WS_2 nanotube was consist of multiple small grains. Moreover, the density functional theory (DFT) simulation showed the edges of WS_2 is metallic, just like the edges of MoS_2. The metallic edges have high density of defect states, which is the recombination states for photogenerated electrons, in between the band gap of WS_2 and MoS_2. Therefore, the WS_2 nanotubes and MoS_2 nanoflakes did not have any photoresponse. Since the WS_2 nanotubes were converted from nanowires, the edges of each tube were not exposed, while this issue does not exist in MoS_2 nanoflakes. Since the electrochemcial active sites are located at the edges, the WS_2 nanotubes did not show as good EC performance as MoS_2 nanoflakes.

Bibliography

[1] Y Feldman, V Lyakhovitskaya, and R Tenne. Kinetics of nested inorganic fullerene-like nanoparticle formation. *Journal of the American Chemical Society*, 120(17):4176–4183, 1998.

[2] R Tenne, M Homyonfer, and Y Feldman. Nanoparticles of layered compounds with hollow cage structures (inorganic fullerene-like structures). *Chemistry of materials*, 10(11):3225–3238, 1998.

[3] Georg Kresse and Jürgen Hafner. Ab initio molecular dynamics for liquid metals. *Physical Review B*, 47(1):558, 1993.

[4] Georg Kresse and Jürgen Hafner. Ab initio molecular-dynamics simulation of the liquid-metal–amorphous-semiconductor transition in germanium. *Physical Review B*, 49(20):14251, 1994.

[5] Georg Kresse and Jürgen Furthmüller. Efficient iterative schemes for ab initio total-energy calculations using a plane-wave basis set. *Physical review B*, 54(16):11169, 1996.

[6] Georg Kresse and Jürgen Furthmüller. Efficiency of ab-initio total energy calculations for metals and semiconductors using a plane-wave basis set. *Computational materials science*, 6(1):15–50, 1996.

[7] John P Perdew, Kieron Burke, and Matthias Ernzerhof. Generalized gradient approximation made simple. *Physical review letters*, 77(18):3865, 1996.

[8] Stefan Grimme, Jens Antony, Stephan Ehrlich, and Helge Krieg. A consistent and accurate ab initio parametrization of density functional dispersion

correction (dft-d) for the 94 elements h-pu. *The Journal of chemical physics*, 132(15):154104, 2010.

[9] Stefan Grimme, Stephan Ehrlich, and Lars Goerigk. Effect of the damping function in dispersion corrected density functional theory. *Journal of computational chemistry*, 32(7):1456–1465, 2011.

[10] Berit Hinnemann, Poul Georg Moses, Jacob Bonde, Kristina P Jørgensen, Jane H Nielsen, Sebastian Horch, Ib Chorkendorff, and Jens K Nørskov. Biomimetic hydrogen evolution: Mos2 nanoparticles as catalyst for hydrogen evolution. *Journal of the American Chemical Society*, 127(15):5308–5309, 2005.

[11] Thomas F Jaramillo, Kristina P Jørgensen, Jacob Bonde, Jane H Nielsen, Sebastian Horch, and Ib Chorkendorff. Identification of active edge sites for electrochemical h2 evolution from mos2 nanocatalysts. *science*, 317(5834):100–102, 2007.

[12] Desheng Kong, Haotian Wang, Judy J Cha, Mauro Pasta, Kristie J Koski, Jie Yao, and Yi Cui. Synthesis of mos2 and mose2 films with vertically aligned layers. *Nano letters*, 13(3):1341–1347, 2013.

[13] MV Bollinger, JV Lauritsen, Karsten Wedel Jacobsen, Jens Kehlet Nørskov, S Helveg, and Flemming Besenbacher. One-dimensional metallic edge states in mos 2. *Physical review letters*, 87(19):196803, 2001.

[14] WJ Schutte, JL De Boer, and F Jellinek. Crystal structures of tungsten disulfide and diselenide. *Journal of Solid State Chemistry*, 70(2):207–209, 1987.

[15] GL Frey, R Tenne, MJ Matthews, MS Dresselhaus, and G Dresselhaus. Optical properties of ms 2 (m= mo, w) inorganic fullerenelike and nanotube material

optical absorption and resonance raman measurements. *Journal of materials research*, 13(9):2412–2417, 1998.

[16] C Ballif, M Regula, PE Schmid, M Remškar, R Sanjines, and F Lévy. Preparation and characterization of highly oriented, photoconducting ws 2 thin films. *Applied Physics A*, 62(6):543–546, 1996.

[17] Wenqing Li, Christian FJ Walther, Agnieszka Kuc, and Thomas Heine. Density functional theory and beyond for band-gap screening: performance for transition-metal oxides and dichalcogenides. *Journal of chemical theory and computation*, 9(7):2950–2958, 2013.

[18] Line Sjolte Byskov, Bjørk Hammer, Jens Kehlet Nørskov, BS Clausen, and Henrik Topsøe. Sulfur bonding in mos 2 and co-mo-s structures. *Catalysis letters*, 47(3-4):177–182, 1997.

[19] Line S Byskov, Jens K Nørskov, Bjerne S Clausen, and Henrik Topsøe. Dft calculations of unpromoted and promoted mos2-based hydrodesulfurization catalysts. *Journal of Catalysis*, 187(1):109–122, 1999.

[20] Charlie Tsai, Frank Abild-Pedersen, and Jens K Nørskov. Tuning the mos2 edge-site activity for hydrogen evolution via support interactions. *Nano letters*, 14(3):1381–1387, 2014.

Chapter 3

Stability and Electronic Properties of Tin Disulfide (SnS_2) Edges

3.1 Introduction

Because of its 2D structure and semiconducting properties, tin disulfide (SnS_2) is of interest for applications in electrochemical catalysis and sensing, as an electron transport layer for photovoltaics, and as an active materials in photodetectors and thin film transistors. Different from 2H-WS_2 and 2H-MoS_2, the crystal structure of SnS_2 could make SnS_2 more efficient in photoelectrochemical (PEC) reaction. The first part of this chapter focuses on experimental synthesis and characterization of SnS_2 nanoflakes that have excellent PEC performance. The second part focuses on the density functional theory (DFT) simulations of atomic and electronic structure of the bulk-like and monolayer SnS2 edges under different chemical conditions. While the atomic and electronic structure of the basal planes of bulk and monolayer SnS_2 are well known, the same is not known for the edges, which could have a major influence on the performance of SnS_2 in the PEC applications. The found of that

the edges of SnS_2 are still semiconducting explains its excellent PEC performance observed in experiments. We also found that the band gap energy of the SnS_2 edges becomes smaller with increasing sulfur coverage, and thereby determined the influence of chemical synthesis conditions on the electronic structure of the edges.

3.2 Experimental and Computational Details

3.2.1 Experimental details

Synthesis of SnS_2 powders

We made SnS_2 powders by hydrothermal reaction. 3M of thiourea (Sigma Aldrich, >99%) and 0.1M tin(IV) chloride pentahydrate (Sigma Aldrich, >98%) were mixed in 40 mL deionized (DI) water, followed by stirring for 30 min. The solution was then transferred to a steel autoclave lined with Teflon for hydrothermal reaction at 180 °C for 24 hours. Then the precipitate was collected and rinsed with ethanol and DI water for several times. The washed precipitate was dried in air at 50 °C first to evaporate remaining ethanol and water followed by further drying at 200 °C in vacuum for 8 hours.

Synthesis of SnS_2 nanoflakes

Flourine-doped tin oxide (FTO) glass (Hartford Glass, IN) substrates were cut into 2 cm × 2.5 cm and sonicated multiple times in a 1:1:1 mixture of isopropanol, acetone, and DI water. After being dried with compressed air, the glass was ready for growth of SnS_2 nanoflakes.

The SnS_2 nanoflakes were made by close-space sublimation (CSS). The CSS system consisted of a quartz tube that had the FTO substrate in the inner upper side

and the SnS_2 powder made by hydrothermol reaction set right below the substrate, and a flat-flame burner underneath the quartz tube. The FTO substrate was connected to a tube in which flows cooling water, so that the temperature of substrate could be kept low enough for nanoflakes growth. The burner was used to provide heat to evaporate SnS_2 powders by igniting CH_4 and air mixture gas. During synthesis, the quartz tube was under high vacuum (around 10 mTorr). By controlling the temperature of SnS_2 powder and the FTO substrate, the synthesis of certain shape (nanowires and nanoflakes) and certain length of SnS_2 nanostructures was achieved [1].

Photoelectrochemical (PEC) measurements

Photoelectrochemical (PEC) measurements for SnS_2 nanoflakes were performed in a three-electrode configuration with Pt wire as the counter electrode and saturated calomel electrode (SCE) as the reference electrode. All voltages were converted to reversible hydrogen electrode (RHE) by

$$V_{RHE} = V_{SCE} + 0.059 \times pH + 0.244. \tag{3.1}$$

N_2 gas and a magnetic stirrer were used for eliminating mass transfer limitations. The sweep rate of linear sweep voltammetry (LSV) measurements was 10 mVs^{-1}. A xenon lamp (model 6258, Oriel) equipped with an AM1.5G gilter (model 81094, Oriel) provided the simulated sunlight for all PEC measurements.

3.2.2 Deposition of Copper (Cu)

Copper particles were deposited on SnS_2 nanoflakes by electrodeposition in 1 M $CuSO_4 \cdot 5H_2O$ with cyclic voltammetry (20 times) from 0.74 to 0.57 VRHE.

Photoluminescence (PL) measurement

The photoluminescence (PL) of SnS_2 was measured using a Hriba IhR550 spectrometer with 405 nm fiber-coupled laser and Horiba Synapse CCD camera.

Characterization

The morphology of nanostructures of WS_2 and MoS_2 were characterized using scanning electron microscopy (SEM) (JEOL 7000F, 10 kV), transmission electron microscopy (TEM) (JEOL 2100, 200 kV), atomic force microscopy (AFM) (NaioAFM, Nanosurf, static force mode), and parallel beam x-ray diffraction (XRD) (PANalytical Empryrean, Cu kα, 45 kV, 40 mA).

Raman spectra were obtained by an XploTa Raman microscope (Horiba Scientific, USA) with a 532 nm laser. The laser light used here was from a 100× magnification lens from Olympus, and a 2400 line grating along with 2 s of accumulation time and 25 repetitions were used to collect the measurement signal.

X-ray photoelectron spectroscopy (XPS) measurements were performed using a Phi 5600 instrument that utilized a monochromated Al Kα anode operating at 13.5 kV and 300 W with photoelectron collection in 25 meV steps at a 23.5 eV pass energy.

3.2.3 DFT simulation details

All of the simulations were utilized with the Vienna ab initio simulation package (VASP) [2, 3, 4, 5]. The convergence criteria of the electronic and ionic relaxations were 10^{-5} eV and 0.01 eV/Å, respectively. A plane wave cutoff energy of 400 eV was used. A 6x6x2 Gamma centered k-point grid was used for lattice optimization of bulk SnS_2. A single k-point was used for bulk-like and monolayer slab calculations

because of the large size of the supercells (as discussed below). The generalized gradient approximation (GGA) with the Perdew-Burke-Ernzerhof (PBE) [6] exchange correlation functional was used for all of the geometry optimizations. For electronic structures including density of states (DOS) and band structure, the Heyd-Scuseia-Ernzerhof (HSE06) hybrid exchange correlation functional [7] was employed, because PBE always underestimated the energy value of band gap. However, because of the larger sizes of the bulk-like and monolayer slabs with exposed edges and the large computational time of HSE06 calculations, we calculated the band structure of bulk-like and monolayer edges with more efficient functional, PBE, which gives very similar results to HSE06. We can see from Figure 3.1 the band structure generated by PBE is very similar to that by HSE06 including the shape of curves and the relevant positions of CBM and VBM. Although PBE underestimates the value of bandgap, we can still study other properties such as the type of bandgap from the plots. The Grimme's zero damping DFT-D3 method [8, 9] was used in all calculations to describe the van der Waals interaction between the layers of SnS_2.

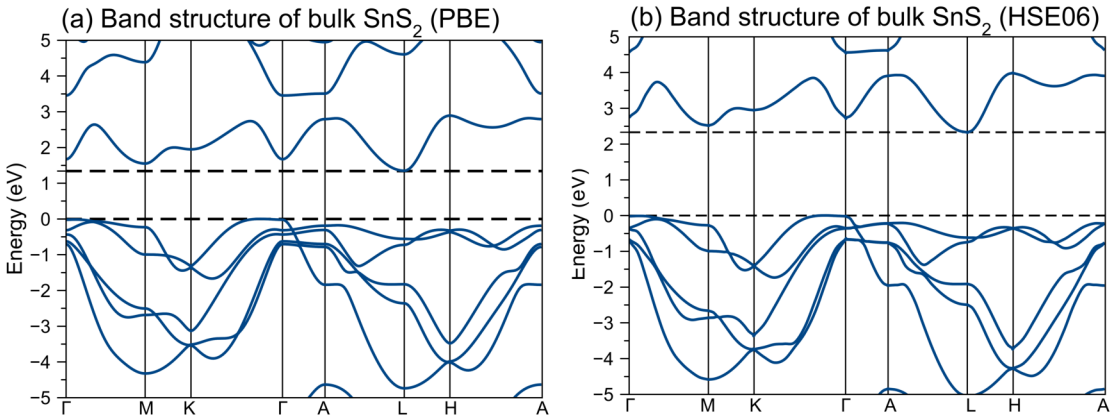

Figure 3.1: Band structures of bulk SnS_2 calculated by PBE (a) and HSE06 (b).

Figure 3.2shows all the cells we simulated in this chapter. The lattice parameters of SnS_2 were determined by geometry optimization of bulk SnS_2 unit

cell(Figure 3.2(a)). Then the cell of monolayer SnS_2 without edges were made from optimized bulk unit cell (Figure 3.2(b)). The slab models of bulk-like slab and monolayer slab with edges exposed were also made by extending optimized bulk unit cell and then cut the slab exposing the edges (Figure 3.2(c) and (d)). The $(10\bar{1}0)$ facet is the most stable edge observed in previous experiments [1, 10], therefore here the $(10\bar{1}0)$ facet was studied here which is shown in Figure 3.2(c) and (d). For both the bulk-like and monolayer edge models, an 8-Sn-layer slab model with around 18 Å vacuum along the z-direction was used so that the middle two layers behaved as bulk SnS_2, while the top and the bottom layers were free surfaces. Different from WS_2, one can find that there were two edges in the slab from Figure 3.2(c) and (d) which were identical, because of the symmetry of crystal structure of SnS_2. Figure 3.2(c) and (d) show the slabs with edges that had no S coverage. For the monolayer slab, the SnS_2 single layer was separated from other planes by a vacuum of 14 Å in the supercell in order to ignore the interaction between two planes.

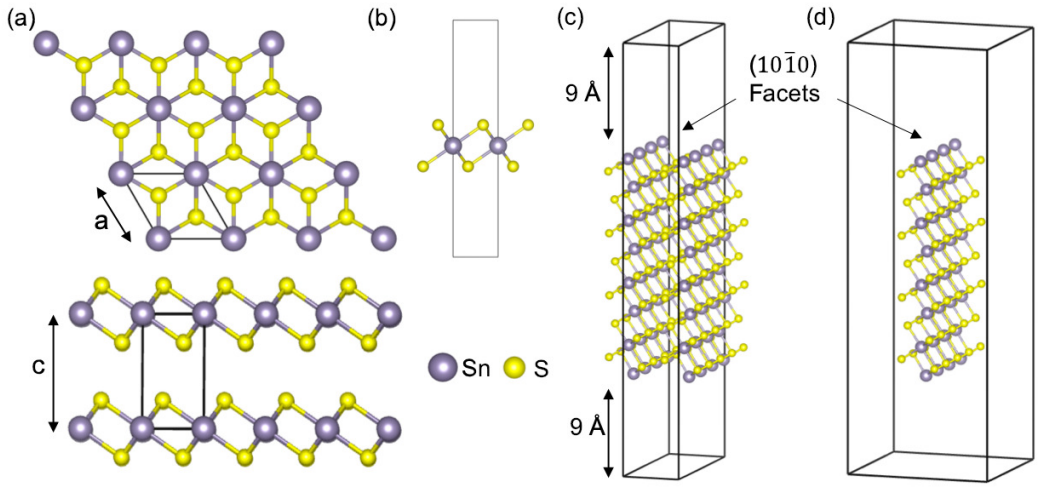

Figure 3.2: The unit cells and super cells of the modeling. Purple balls represent Sn atoms and the yellow balls are S atoms. (a) is the top and side views of bulk SnS_2; the solid line is the unit cell; (b) is the side view of the unit cell of monolayer SnS_2; (c) is the the super cell of bulk-like SnS_2 slab model with edges exposed; (d) is the super cell of monolayer SnS_2 slab model with edges exposed.

3.2.4 Thermodynamic calculations

A primary goal of this part of work was to determine the atomic arrangement/configurations of S atoms at the SnS_2 edges. To determine the most stable edges of SnS_2 under various environmental conditions, surface free energies was calculated using DFT results of the bulk-like and monolayer SnS_2 edges (similar to previous work [11, 12, 13, 14]). The surface free energy, γ^i, of the slab with i termination can be determined by:

$$\gamma^i = \frac{(G^i_{surf} - N_{Sn}\mu_{Sn} - N_S\mu_S)}{2A}. \tag{3.2}$$

A is the area of the surface. The A value for the bulk-like slab was taken from the cell lattices parallel to the surface, since the exposed surface all fits within the simulation cell. Finding the A value for the monolayer slab was more complicated since there as vacuum above the surface and perpendicular to the single layer. There is no unambiguous way to define surface area for the monolayer. We took the monolayer's atomic coordinates and added the van der Waals radius to each atom. The area could then be found by measuring the distance from van der Waals radius edge to van der Waals radius edge. N_{Sn} and N_S are the number of Sn and S atoms in the slab. μ_{Sn} and μ_S are the chemical potentials of Sn and S in the slab. The free energy of the surface slab can be approximated by E^i_{slab}, the DFT-calculated energy, since pV and entropy terms are typically small for solids. Such an approach is similar to previous work [14].

The chemical potentials of Sn and S can be written in terms of the bulk SnS_2 chemical potential, μ_{SnS_2}:

$$\mu_{SnS_2} = \mu_{Sn} + 2\mu_S. \tag{3.3}$$

Neglecting entropy and pV for the bulk (and slabs) since again they are typically negligible, μ_{SnS_2} could be approximated as $E^{bulk}_{SnS_2}$, where $E^{bulk}_{SnS_2}$ is the DFT energy

of bulk SnS_2. Therefore, using Equation (3.3) to eliminate μ_{Sn} in equation (3.2) the following was obtained:

$$\begin{aligned} \gamma^i &= \frac{1}{2A}[E^i_{slab} - N_{Sn}(E^{bulk}_{SnS_2} - 2\mu_S) - N_S\mu_S] \\ &= \frac{1}{2A}[E^i_{slab} - N_{Sn}E^{bulk}_{SnS_2} - \mu_S(N_S - 2N_{Sn})]. \end{aligned} \tag{3.4}$$

From Equation (3.4) one can see that the surface free energy is dependent on μ_S.

At equilibrium, the value of μ_S becomes constrained, as discussed in similar work[15]. When μ_S becomes too low, sulfur atoms would leave the bulk material and the SnS_2 would break down into solid Sn and S. The maximum value of the Sn chemical potential corresponds to bulk Sn:

$$\mu_{Sn}(T,p)[max] \approx E^{bulk}_{Sn}(T,p). \tag{3.5}$$

Since μ_S and μ_{Sn} are constrained by Equation (3.3), one can find the minimum possible value of μ_S by:

$$\begin{aligned} \mu_S[min] &= \frac{1}{2}[\mu^{bulk}_{SnS_2} - \mu^{bulk}_{Sn}(max)] \\ &\approx \frac{1}{2}(E^{bulk}_{SnS_2} - E^{bulk}_{Sn}). \end{aligned}$$

$E^{bulk}_{SnS_2}$ is the total energy per SnS_2 unit, while E^{bulk}_{Sn} is the energy per Sn atom for α-Sn bulk. If the S chemical potential drops below this value, bulk SnS_2 would break apart into S and Sn. S_2 was a reference species for the maximum value of the S chemical potential, since gas-phase sulfur is often used for SnS_2 synthesis [14]. The maximum value of μ_S will be equal to $\frac{1}{2}E_{S_2}$:

$$\mu_S[max] = \frac{1}{2}E_{S_2}. \tag{3.6}$$

Above this value the S atoms would form S_2 gas instead of staying on the SnS_2 edges. Introducing $\Delta\mu_S = \mu_S - \frac{1}{2}E_{S_2}$, the range of chemical potentials for S is:

$$\frac{1}{2}[E^{bulk}_{SnS_2} - E^{bulk}_{Sn} - E_{S_2}] < \Delta\mu_S < 0, \tag{3.7}$$

In summary, the surface free energy of different edge terminations can be found by:

$$\gamma^i = \frac{1}{2A}[E^i_{slab} - N_{Sn}E^{bulk}_{SnS_2} - (N_S - 2N_{Sn})(\Delta\mu_S + \frac{1}{2}E_{S_2})]. \tag{3.8}$$

Plugging in the exact values, the range of the chemical potential of S is:

$$-1.31eV \leq \Delta\mu_S \leq 0eV. \tag{3.9}$$

In order to relate the simulation work to real experimental conditions, the S chemical potentials to sulfur gas at finite temperature and pressure were correlated. According to previous studies[16, 17], sulfur gas molecules exist as S_2 to S_8, or a mixture of several species at different temperatures and pressures. At high temperatures and low pressures (which are often used during synthesis), smaller S molecules dominate, especially S_2[18, 16]. Therefore S_2 was used as a reference molecule here. The chemical potentials at different temperatures were calculated using this equation [15]:

$$\mu_S(T,p) = \mu_S(T,p^\circ) + \frac{1}{2}kTln(\frac{p}{p^\circ}), \tag{3.10}$$

where k is the Boltzman constant and $\mu_S(T,p^\circ)$ is the chemical potential per atom of S_2 gas at a reference pressure p°. The chemical potential can also be determined

by

$$\mu_S(T, p^\circ) = \frac{1}{2}\mu_{S_2}(0K, p^\circ) + \frac{1}{2}\Delta G(\Delta T, p^\circ, S_2). \quad (3.11)$$

Since $\mu_S(0K) = \frac{1}{2}E_{S_2}$, we have

$$\begin{aligned}\mu_S(T, p^\circ) &= \frac{1}{2}E_{S_2} + \frac{1}{2}[H(T, p^\circ, S_2) - H(0K, p^\circ, S_2)] \\ &\quad -\frac{1}{2}T[S(T, p^\circ, S_2) - S(0K, p^\circ, S_2)] \end{aligned} \quad (3.12)$$

where $\Delta G(\Delta T, p^\circ, S_2)$ is Gibbs free energy of S_2 gas at pressure p°. The JANAF thermochemical data[19] was used for entropy and enthalpy values used in Equation (3.12). According to JANAF thermochemical data, the reference pressure p° was used here is 0.1 MPa.

3.3 SnS_2 nano-flakes

To achieve edge-rich vertical SnS_2 nanoflakes, the vertical stepped layers of SnS_2 nanoflakes were grown by CSS in vacuum (Figure 3.3(d)). From Figure 3.3 (a) one can clearly see the steps of the nanoflakes. According to AFM height profile, the height of the edge of the nanoflakes was not uniform, i.e. the edge of the flakes has multiple height, which also proves the fact that the nanoflakes have stepped structure. The steps were formed due to nucleation and growth of new basal planes onto the sides of the existing basal planes at high gas concentrations (high supersaturations) or due to the interaction of neighboring nanoflakes during the prolonged growth. This is different from CVD-grown vertical SnS_2 nanoflakes [20], in which the gas concentration was elatively low, resulting in low supersaturation and no nucleation on the sides of the existing basal planes. TEM selected area electron

diffractio (SAED) pattern (Figure 3.3(d)) shows the d-spacing of (100) plane is 3.16 Å. XRD and Raman results also match with those of 2H-SnS_2, which provide extra evidence for the crystal structure of our SnS_2 are the common 2H phase.

The stepped-layer structure provided more edges that can be involved in photoelectrocatalysis reactions. In other words, the stepped-layer structure had additional active sites for PEC and therefore can boost the overall photocurrent. The photoelectrocatalysis performance of the SnS_2 nanoflakes is the best among all known SnS_2 photoelectrocatalysts [20]. The highest photocurrent that the SnS_2 nanoflakes achieved was 4.5 mA cm^{-2} at 1.23 V_{RHE} in phosphate buffer and 1 M Na_2SO_3 (see Figure 3.4 (a)), since Na_2SO_3 is a hole scavenger with fast oxidation kinetics. Since Na_2SO_4 is one of commonly used electrolytes for water oxidization, The same performance for the nanoflakes was measured in 0.5 M Na_2SO_4 and got 2.6 mA cm^{-2} of photocurrent for water oxidation. This was 1.7 times larger than the photocurrent of CVD-grown SnS_2 nanoflakes, and much higher than the 0.9 mA cm^{-2} of photocurrent of spin-coated horizontal SnS_2 [20].

On the other hand, the photoexcited carrier life of the SnS_2 nanoflakes was measured by time resolved PL (TRPL) decay of the 2.11 eV peak (the band gap energy of the SnS_2 nanflakes measured in the experiment) after exciting with 405 nm laser at near 1 sun peak excitation intensity (around 128 mW/cm). According to TRPL results (see Figure 3.4(b)), the SnS_2 nanoflakes has as high as 1.3 ns of photoexcited carrier life time. The longer photoexcited carrier life time means lower carrier recombination rate. Therefore, comparing to the 0.25 ns photoexcited carrier life time of single crystal SnS_2 [1, 21], the edge-rich SnS_2 nanoflakes had lower carrier recombination rate. Besides, the photoexcited carrier life time of bulk MoS_2 is around 0.69 ns [22]. This is another evidence of that the the semiconducting edges make the carrier recombination rate smaller.

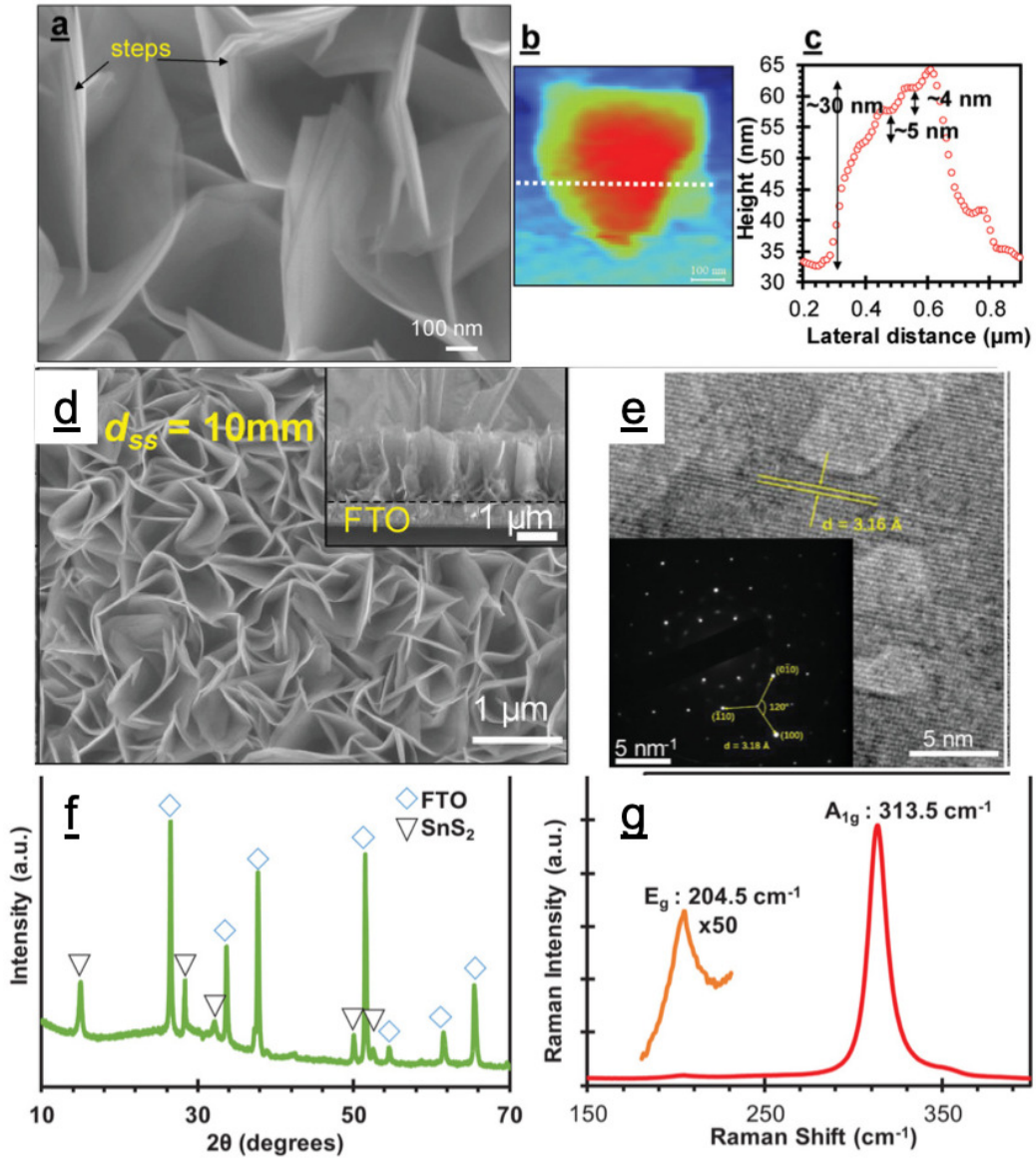

Figure 3.3: Characterization of SnS_2 nanoflakes. (a) SEM image of SnS_2 nanoflakes. The step-structure is very clear here. (b) AFM image of a broken piece of SnS_2 nanoflake. (c) AFM height profile of the corresponding nanoflake. (d) SEM images of top view of SnS_2 nanoflakes. The inset is the corresponding side view of the nanoflakes. (e) High-resolution TEM images of a SnS_2 nanoflake. The inset is the corresponding selected area electron diffraction (SAED) pattern. (f) XRD pattern of SnS_2 nanoflakes on FTO glass. (g) Raman spectroscopy of SnS_2 nanoflakes.

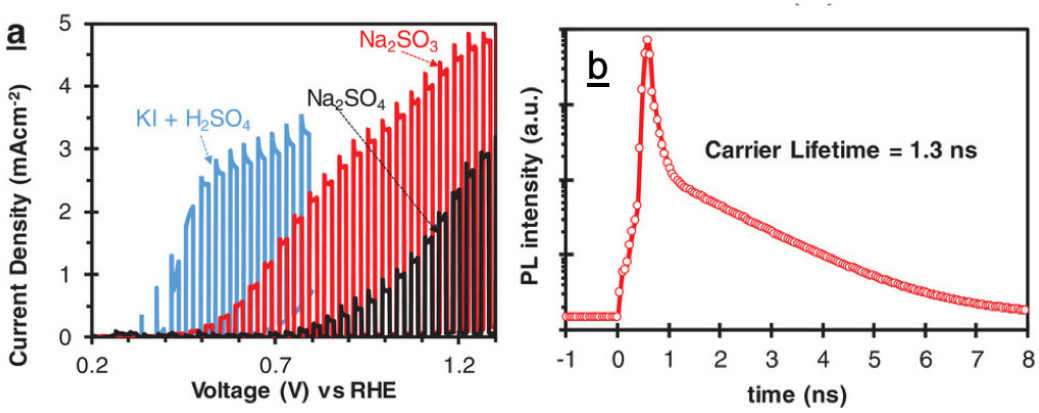

Figure 3.4: (a) PEC measurements of SnS_2 in KI + H_2SO_4, Na_2SO_3, and Na_2SO_4 solutions with back illumination. (b)Light-harvesting efficiency (LHE) of SnS_2 nanoflakes.

Since the synthesis were under high vacuum condition, XPS was used here to investigate the surface of the SnS_2 nanoflakes. The results are shown in the Figure 3.5. As-grown SnS_2 nanoflakes contain S and Sn atoms only according to the XPS (Figure 3.5(a)), while after PEC tests in sulfuric acid the surface of the nanoflakes show significant anodic dissolution (Figure 3.5(b)) . Similarly, the tests in phosphate buffer undergo surface oxidation (Figure 3.5(c)). This suggests that the SnS_2 nanoflakes were not oxidized during synthesis or subsequent exposure to air. However, the edges were dissolved or oxidized during the PEC water oxidation.

During the photoelectrocatalysis measurements we also observed that the edges of the SnS_2 nanoflakes are the active sites. The Cu particles were deposited on top of the edges of nanoflakes/steps by electrochemical reduction (see Figure 3.6), which demonstrated that the edges were more active than the other regions of the nanoflakes. This is not surprising considering the edges were catalytic active sites of 2H-MoS_2 which is reported in previous study [23]. Again, the stepped-layer structure of our SnS_2 nanoflakes provided more edges than CVD-grown ones, which leaded to much higher photocurrent production of our stepped-layer SnS_2 nanoflakes.

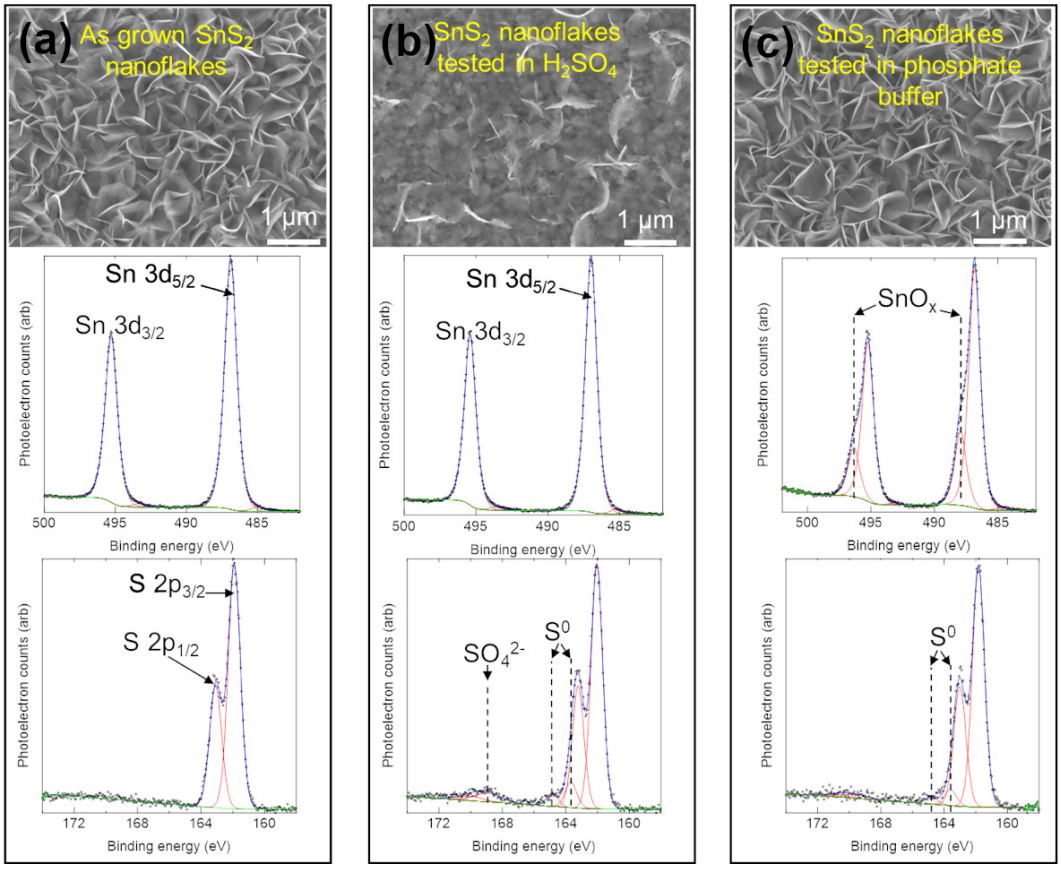

Figure 3.5: XPS images of SnS_2 nanoflakes. (a) as-grown SnS_2 nanoflakes; (b) SnS_2 nanoflakes tested in H_2SO_4 solution; and (c) SnS_2 nanoflakes tested in phosphate buffer. The first row are the SEM images. The second and the third row are the corresponding XPS signal from Sn 3d orbital and S 2p orbital, respectively.

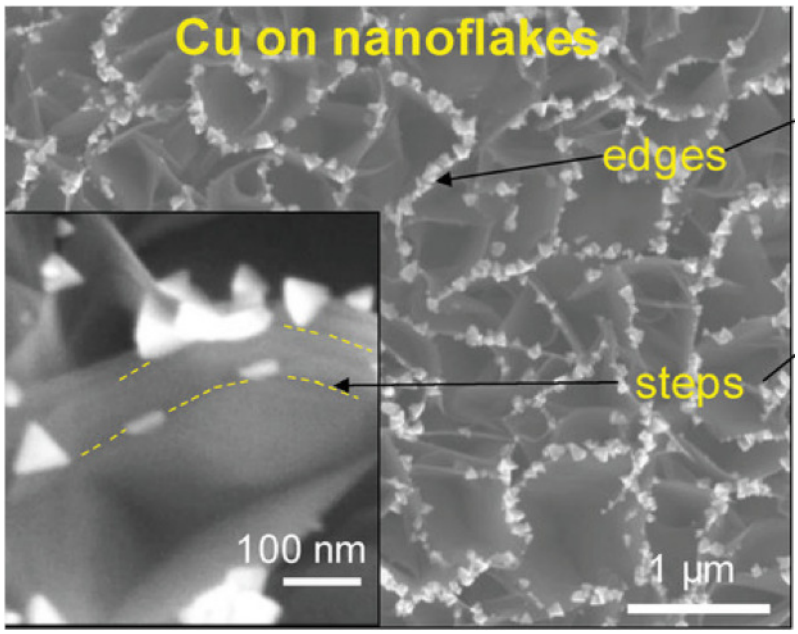

Figure 3.6: SEM images of SnS_2 with Cu particles deposited by reduction, highlighting the edges and steps on the nanoflakes.

3.4 DFT simulation of bulk and monolayer SnS_2 with no edges

Although the SnS_2 nanoflakes had excellent photoelectrocatalysis performance, the atomic configurations of the SnS_2 edges have not been studied. Density functional theory (DFT) simulations were used here to study atomic structure and electronic properties of SnS_2 edges.

The unit cells of bulk and monolayer SnS_2 are shown in Figure 3.2(a) and (b). The bulk lattice parameters calculated here were a = b = 3.69 Å, c = 5.94 Å, which agreed with previous experimental (a = 3.65 Å, c = 5.90 Å) [24] and simulation (a = 3.66 Å, c = 5.81 Å) [25] results. The band gap energy of bulk SnS_2 was 2.34 eV where the conduction band minimum (CBM) is located at the L point and the valence band maximum (VBM) is located between the M and Γ point [26] (see Figure 3.7 (a) and (b)). According to our calculations, the band gap energy of

monolayer SnS_2 was 2.44 eV, or only 0.1 eV larger than that of bulk SnS_2 [27, 26], and monolayer SnS_2 was an indirect semiconductor where the CBM is located at the M point and VBM is located between the Γ and M points. Both monolayer and multilayer SnS_2 have indirect bandgaps according to previous studies [21, 26]. Similar to previous DFT studies [24, 26] the valence and conduction bands were composed of hybridized orbitals for both bulk and monolayer SnS_2. The projected DOS of bulk and monolayer SnS_2 are shown in Figure 3.7(c) and (d). The conduction bands of both bulk and monolayer were composed of Sn *s* and S *p* orbitals, while the valence bands of both bulk and monolayer SnS_2 were both dominated by S *p* and Sn *d* orbitals. The band structures (Figure 3.7(a) and (b)) show that both bulk and monolayer SnS_2 have indirect band gaps, which is in contrast to MoS_2 which has an indirect band gap in the bulk, but a direct bandgap when it becomes a monolayer[28, 21]. These results agree with previous literature on what is known about SnS_2, and also show that both bulk and monolayer SnS_2 have similar properties.

3.5 SnS_2 edge simulations

3.5.1 S arrangement at the edges

There are various possible arrangements of SnS_2 edges with regards to S positions. The bulk-like and monolayer slabs are shown in Figure 3.2 (c) and (d), respectively, with the $(10\bar{1}0)$ facets exposed. The edges shown here had 0% S coverage, meaning only Sn atoms were exposed to the surface. Depending on the S coverage, the edges may have under-coordinated Sn atoms. Each Sn atom in the bulk has a coordination number of 6, while at 0 % S coverage the Sn atoms at the edges have 3 dangling bonds. At 100% S coverage each Sn bonds to 3 surface S atoms, to have a full coordination number of 6.

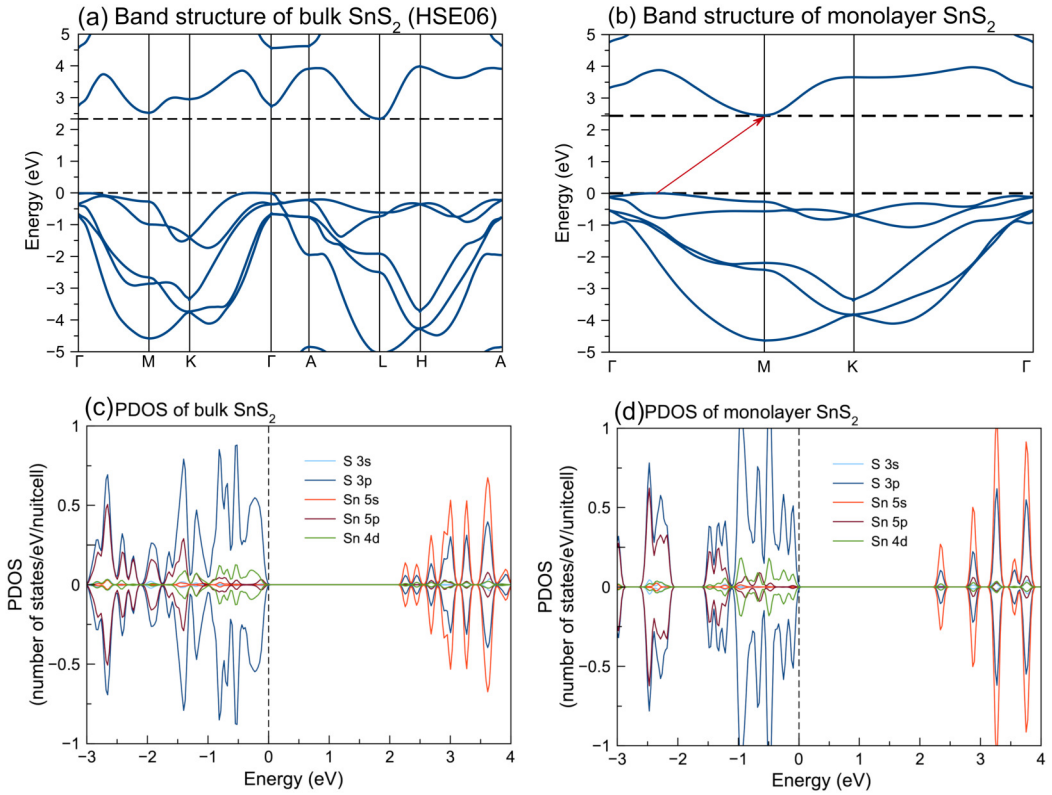

Figure 3.7: Band structure of bulk SnS_2 (a) and monolayer SnS_2 with no edges (b). Projected DOS (PDOS) of bulk SnS_2 (c) and monolayer SnS_2 with no edges (d). All these data are simulated by HSE06 functional.

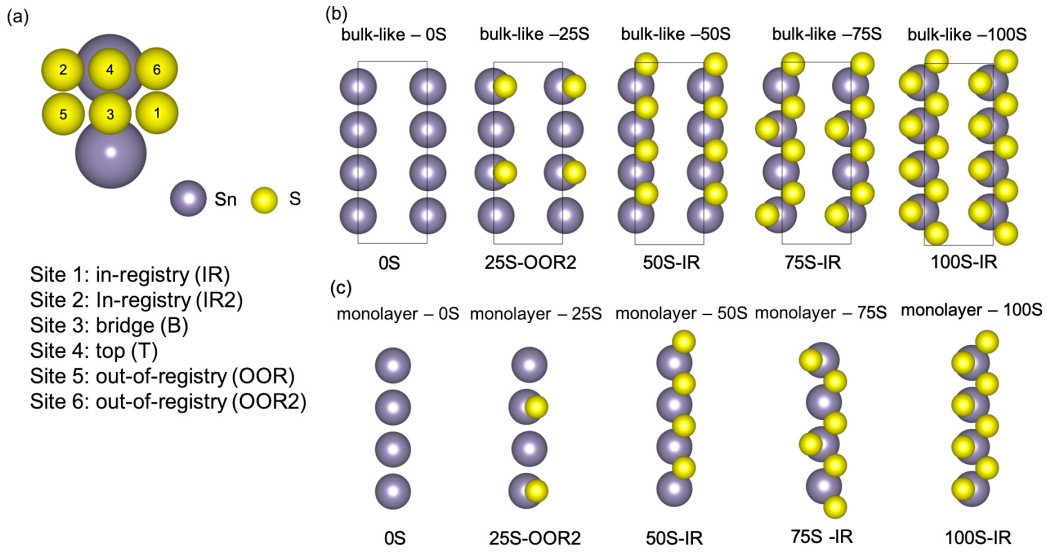

Figure 3.8: (a) Different possible S positions on the surface terminations for every two Sn atoms at the edge. Top views of the most stable configurations at different S coverages for (b) bulk-like edges and (c) monolayer edges. Indicated are the final converged configurations of the S atoms.

There are six possible sites for S atoms at the $(10\bar{1}0)$ edges, as Figure 3.8 shows. Sites 1 and 2 correspond to positions occurring in bulk SnS_2, and were named in-registry site 1 (IR1) and in-registry site 2 (IR2), because the two sites are in registry with the S atoms in the basal plane. That is to say, if one cuts bulk SnS_2 and does not allow relaxation, the S atoms would be in IR1 and IR2 sites. Site 3 bridges two Sn atoms, and as named a bridge site (B). Site 4 is directly on top of a Sn atom, and as named the top site (T). Site 5 and site 6 are the sites that are at the opposite positions of IR1 and IR2, and were named out-of-registry site 1 (OOR1) and out-of-registry site 2 (OOR2). There were 4 Sn atoms at each edge, and 8 S atoms would be equivalent to full (100S) coverage. In other words, 8 S atoms at an edge corresponds to 100% S coverage, while 6 S atoms corresponds to 75% S coverage, etc. Edges with 0%, 25%, 75%, and 100% S coverage for both bulk-like- and monolayer-SnS_2 slabs were modeled. A slab with 50% S coverage is a fully

Table 3.1: Adsorption energies (eV) and optimized surfce configurations for bulk-like and monolayer SnS_2 slabs up to 100% S coverage. Initial and final (after geometry optimization) configurations are indicated. Adsorption energies were calculated using Equation 3.14. The nomenclature for edge configurations are given in Figure 3.8(a). Certain edge configurations did not converge after several thousand geometry optimization steps, and are indicated by dashes.

	bulk-like edges			Monolayer edges		
Initial	Final	Adsorption energy	Total adsorption energy	Final	Adsorption energy	Total adsorption energy
100S-IR	100S-IR	0.23	1.84	100S-IR	0.31	2.48
100S-OOR	–			–		
75S-IR	75S-IR	-0.10	-0.6	75S-IR	-0.02	-0.12
75S-IR2	75S-IR2	0.24	1.44	–		
75S-OOR	–			–		
50S-IR	50S-IR	-0.72	-2.88	50S-IR	-0.64	-2.56
50S-IR2	50S-OOR2	0.06	0.24	50S-OOR2	0.13	0.52
50S-OOR	–			–		
50S-OOR2	50S-OOR2	0.06	0.24	50S-OOR2	0.13	0.52
50S-B	50S-IR	-0.72	-2.88	50S-IR	-0.64	-2.56
50S-T	50S-OOR2	0.06	0.24	50S-OOR2	0.13	0.52
25S-IR	25S-IR	0.28	0.56	25S-IR	0.38	0.76
25S-IR2	25S-OOR2	-0.32	-0.64	25S-OOR2	-0.23	-0.46
25S-OOR	25S-OOR	0.79	1.58	25S-IR	0.38	0.76
25S-OOR2	25S-OOR2	-0.32	-0.64	25S-OOR2	-0.23	-0.46
25S-B	25S-IR	0.29	0.58	25S-IR	0.38	0.76
25S-T	25S-OOR2	-0.32	-0.64	25S-OOR2	-0.23	-0.46
0S	0S	0	0	0S	0	0

stoichiometric slab (SnS_2). Two different sites could be occupied at the same time when the S coverage at an edge was more than 50%. For example, 75% S covered edges could have both IR and OOR sites occupied at the same time. In this case if there are more IR-S atoms than OOR-S atoms, this would be called a 75S-IR edge. If there are more OOR-S than IR-S atoms this would be called a 75S-OOR edge. A range of S coverages and also several possible initial configurations of the S atoms at the edges are summarized in Table 3.1.

To determine the most stable edge configurations for each S coverage, the S

adsorption energies were calculated at 0 K using the reaction:

$$0S + \frac{x}{2}S_2 \rightarrow yS. \tag{3.13}$$

where 0S is the bulk-like or monolayer slab at 0% S coverage (no S on the surface). yS is the bulk-like or monolayer slab at y% (y = 25, 50, 75, and 100) S coverage. x is the number of S atoms added to the surface of the yS slab. S_2 was chosen as a reference S molecule in the vapor phase for consistency. According to the reaction 3.13, the adsorption energies of S were calculated by the following equation:

$$E(adsorption)_{(yS)} = \frac{E_{yS} - E_{0S} - \frac{x}{2}E_{S_2}}{x}. \tag{3.14}$$

E_{yS} is the total energy of the slabs at y% S coverage. x is the number of sulfur atoms adsorbed at the edges. E_{S_2} is the total energy of a S_2 molecule. The adsorption energies were normalized by the number of S atoms added to the surfaces, so that the final formation energy will be in eV/atom.

Table 3.1 indicates all of the configurations before and after relaxation, and their adsorption energies. Several possible initial configurations (6 different initial configurations for 25S, 6 for 50S, 3 for 75S and 2 for 100S) were attempted as mentioned in section 3.5. The final configurations were also indicated. On some edges the S atoms rearranged to form different structures than the initial configurations. For example, the 50S-IR2 configuration converged to the 50S-OOR2 configuration after geometry optimization. Some initial configurations did not converge after more than several thousand geometry steps, indicating those configurations are not likely stable.

The results show that the most stable configurations at each different S coverages were 25S-OOR2, 50S-IR, 75S-IR, and 100S-IR, which are shown in Figure 3.8. Furthermore, the 50S-IR edges were the most stable for both bulk-like and monolayer

edges at 0 K, as given by the lowest total adsorption energy (adsorption energy per atom multiplied by the number of S atoms adsorbed). This is the stoichiometric surface, so from a chemistry viewpoint should be very stable. Besides, the higher coverage surfaces were not stable or only weakly stable. For several of the high coverage surfaces (i.e. 100S) during the geometry optimization, S_2 molecules would occasionally leave the surface, dissociating from the SnS_2 surface. This reinforces the notion that high coverage of S is unstable on the SnS_2 edges. These results show that, in general, S atoms were more likely to occupy the in-registry sites of the edges, with the exception of OOR2 sites being more favorable over the 25S surfaces. IR-S atoms have the same positions as S atoms in bulk SnS_2, which explains why they are so stable when adsorbed on the surfaces. In addition, the fact that the stable edge configurations of bulk-like slabs and monolayer slabs were the same suggests that the van der Waals force between SnS_2 layers do not significantly affect the edge configurations.

3.5.2 Thermodynamic considerations of edge structures

To determine the relative stability of different surfaces as a function of S chemical potential, which can be related to finite temperature and pressure, thermodynamic analysis was involved. The surface free energy as function of S chemical potential was calculated for both bulk-like and monolayer SnS_2 slabs using Equation (3.4). These results are plotted in Figure 3.9.

The slope of each surface grand potential line was determined by $\frac{N_S-2N_{Sn}}{2A}$, as rearranging Equation 3.8 shows:

$$\gamma^i = \frac{1}{2A}[E^i_{slab} - N_{Sn}E^{bulk}_{SnS_2}] + \frac{(N_S - 2N_{Sn})}{2A}\frac{1}{2}E_{S_2} - \frac{(N_S - 2N_{Sn})}{2A}\Delta\mu_S. \quad (3.15)$$

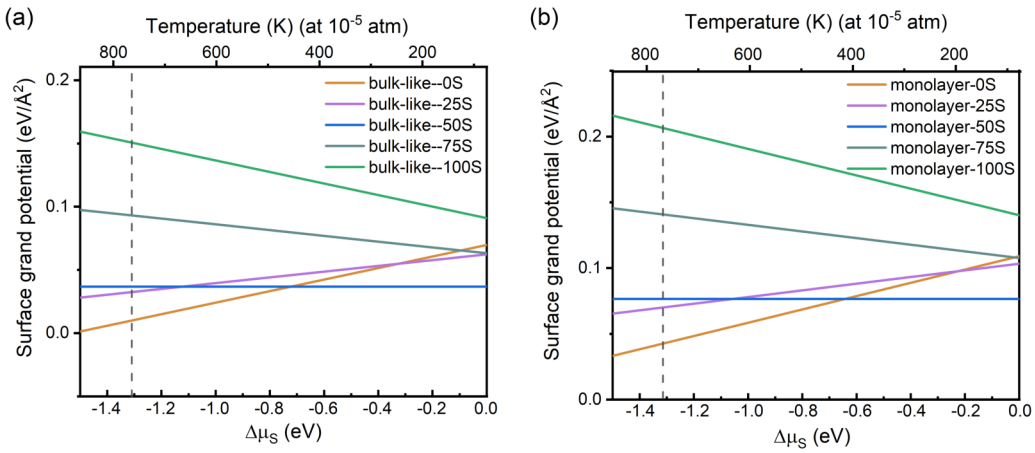

Figure 3.9: Surface free energies of bulk-like edges (a) and monolayer (b) SnS_2 slabs at different S chemical potentials. The corresponding temperatures (top x-axis) are determined by the chemical potential of S_2 gas at 10^{-5} atm. Viable chemical potentials, $\Delta\mu_S$, are between -1.31 and 0 eV, as explained in Methodology.

Because of this slope, the surfaces with more sulfur atoms (N_S) had more negative slopes and become more favorable with increasing sulfur chemical potential. The lines with negative slope correspond to the edges with excess S atoms (75S and 100S), while those with positive slope correspond to the edges with excess Sn atom (0S and 25S), and slope is 0 correspond to stoichiometric structure (50S). Therefore 75S and 100S are more stable in the sulfur rich region and other edges are more favorable in the sulfur poor region.

The edge with the lowest surface free energy is the most stable edge at a given S chemical potential. Hence, from Figure 3.9 one can conclude that bulk-like and monolayer SnS_2 edges will adopt a 0S coverage at low $\delta\mu_S$ and 50s coverage for higher $\delta\mu_S$ values. 75S and 100S coverages are not stable at any of the chemical potential ranges. Interestingly, the 25S was also not stable, so that the coverage jumps from 0 to 50S abruptly. The most stable arrangement of S atoms for the 25S edge had S atoms in the OOR2 arrangement, unlike any other surface, which could explain why 25S coverage would not be observed for these slabs. The bulk-like and

multilayer edges had similar free energies according to the plots, which also suggests that the interactions between layers do not affect surface stability.

To understand these results in the context of sulfur at different temperatures and pressures, the molecular sulfur at 10^{-5} atm was chosen as a reference state. In the previous experiments[1] the SnS_2 nanoflakes were synthesized at 723 K and 10^{-5} atm which corresponds to $\Delta\mu_S$ of -1.2 eV. The corresponding temperatures of S_2 molecules at 10^{-5} were given in the upper x-axis of Figure 3.9. Table B.1 provides $\delta\mu_S$ values for a range of pressures and temperatures that may correspond to a variety of other environmental conditions. This allows connection of the calculated surface grand potential to experiments. According to Figure 3.9 the most stable nanoflakes that we synthesized in our previous work[1] would have 0% S covered edges, at least during synthesis. If the flakes could be synthesized at lower temperatures, then 50S edges may form, but at lower temperatures diffusion limitations may affect nanoflake synthesis.

Other sulfur molecules were also considered considering the complexity of the sulfur species in the sulfur vapor. In reality sulfur gas will be a mixture of different molecules [16], and depending on temperature/pressure, different sulfur molecules will dominate the gas phase. Table B.2 shows chemical potentials for S_8. Unlike S_2, the chemical potentials span a very narrow range, and in the presence of S_8 the SnS_2 surface would adopt a 50S termination, except for very high temperatures.

3.5.3 Electronic properties of the edges

As mentioned in Chapter 2, the zero photocurrent of WS_2 and MoS_2 is due to the metallic edges. Then the electronic structure of SnS_2, who has excellent PEC performance, is even more critical, since this will provide more evidence on the relation between conductivity and charge recombination rate. The calculated DOS

and band structures of the most stable bulk-like and monolayer SnS_2 edges (as determined in Chapter 3.5) are presented here. Figure 3.10 shows the density of states of bulk-like and monolayer SnS_2 edges. The atoms in the top 7th to 8th atomic layers were taken as edge atoms, and used to obtain the DOS and band structure of the edges (see Figure 3.10 (d)). Figure 3.10 shows that the band gap energies of the edges were smaller than the band gap energy of bulk SnS_2 (2.34 eV), and that the band gap energy decreased with increasing S coverage. The band gap energies of both bulk-like- and monolayer-0S and 50S edges were slightly smaller than those of the bulk and monolayer SnS_2 without edges, while the band gap energies of 100S edges were around 0.7 eV smaller than that of the bulk and monolayer SnS_2 without edges. These results show that by controlling the S coverage of the edges of SnS_2 flakes, the band gap energy of the edges can be controlled, which may modulate photo-absorption behavior. According to the DOS plots, the edges of SnS_2 are still semiconducting, no matter the S coverage. This is in contrast to the metallic edges of typical 2D sulfides, such as 2H-MoS_2 [29, 30]. The charge recombination rate at the semiconducting edges could be smaller than at metallic edges, explaining why SnS_2 is a promising photovoltaic and photoelectrocatalytic material. Furthermore, the semiconducting edges of SnS_2 could avoid the short circuit issue that MoS_2 might have in FETs. Table 3.2 summarizes the band gap energies and band gap types of bulk, bulk-like edges, monoaleyr with no edges, and monolayer edges obtained by both HSE06 and PBE.

Direct-band gap semiconductors have better photoluminescence [28] and may be more suitable in photovoltaic applications due to higher photoabsorption [31, 32]. The bulk-like and monolayer-50S edges are unlike the basal planes, in that they both have direct band gaps, (Figure 3.11), while bulk-like and monolayer-0S and 100S edges have indirect band gaps. This is important, because it indicates that

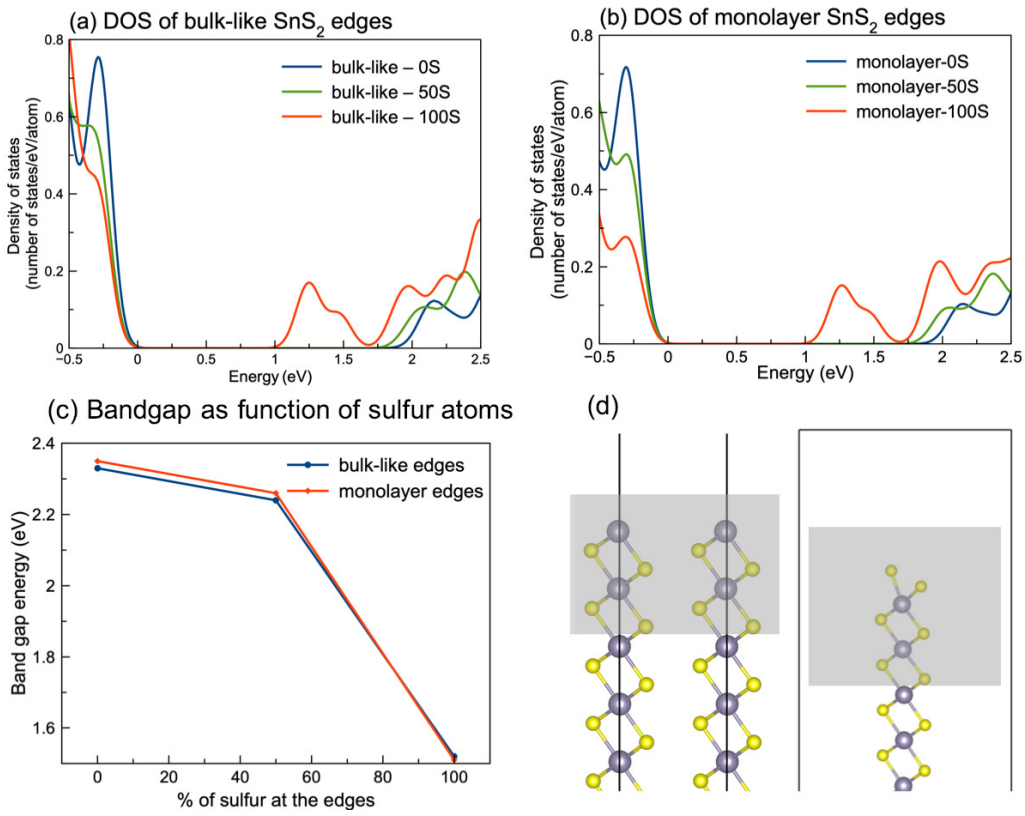

Figure 3.10: Density of states of (a) bulk-like and (b) monolayer SnS_2 edge atoms as calculated using the HSE06 functional. The valence band edge is set at 0 eV. (c) The band gap energy as a function of sulfur coverage. For reference, the calculated band gaps of multilayer (bulk) SnS_2 and monolayer SnS_2 (no edges) are 2.34 and 2.44 eV. (d) Side view of bulk-like and monolayer slabs. Grey lines indicate the cell edges. The shaded atoms were used to calculate the DOS representing edge atoms.

photoabsorption should be enhanced at the 50 S edges compared to bulk SnS_2 or at the basal planes. However, 50 S edges may also enable more facile charge recombination, which could be detrimental. These results indicate that the band electronic properties can be modulated by controlling the edge configurations.

3.5.4 H adsorption at the edges

The edges of SnS_2 may be especially reactive sites for photocatalysis or electrocatalysis, especially when compared to the basal planes. Hydrogen dissociative adsorption

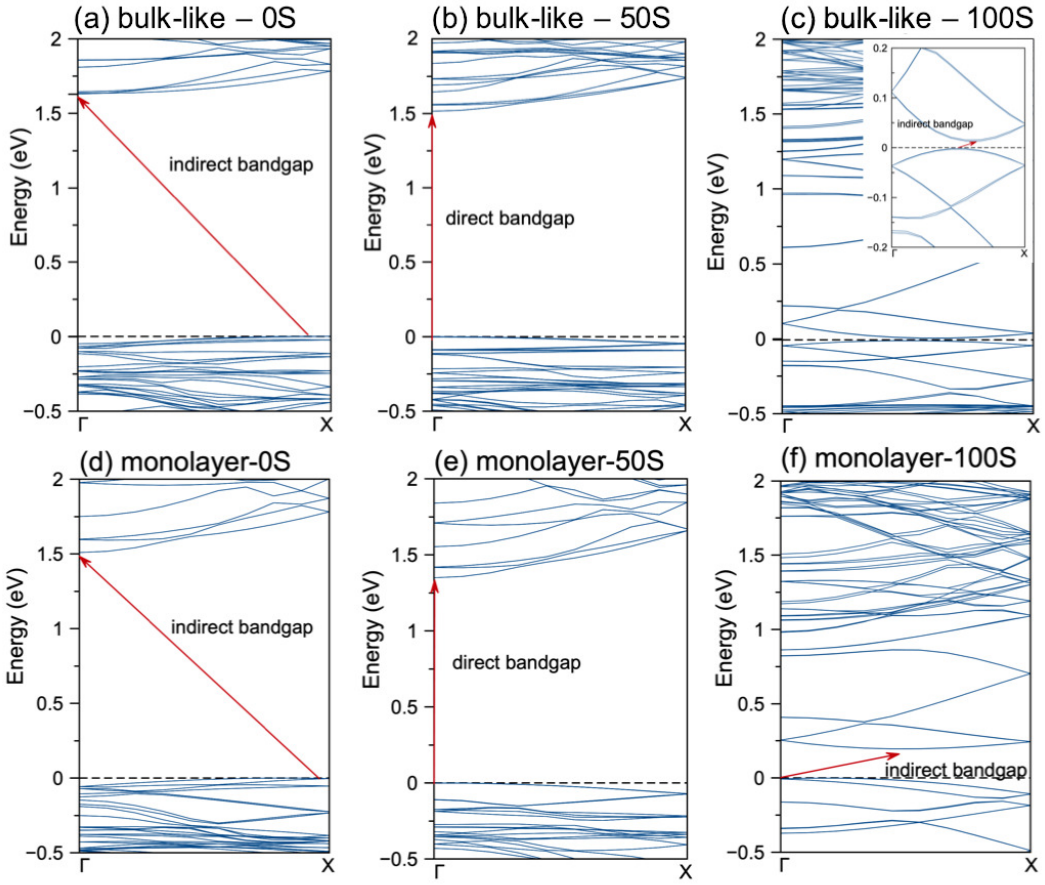

Figure 3.11: Calculated band structures of mulitlayer and monolayer slabs. The valence band maximum are set at 0 eV. The inset of (c) shows a zoomed in region of the band gap. Results are from using the PBE functional, which is why band gaps are underestimated. As discussed in the Methodology, PBE and HSE06 give qualitative agreement for band structures (see Figure S1), even if PBE underestimates band gaps.

Table 3.2: Calculated band gap energies (E_{gap} in eV) and types for SnS_2 edges. The band gap energies were extracted from the eigenvalues of the DFT simulations.

		E_{gap} [HSE06]	E_{gap} [PBE]	band gap type
bulk-like	bulk SnS_2	2.33	1.34	indirect
	edge-0S	2.33	1.53	indirect
	edge-50S	2.24	1.41	direct
	edge-100S	1.52	0.11	indirect
monolayer	monolayer with no edge	2.43	1.59	indirect
	edge-0S	2.35	1.64	indirect
	edge-50S	2.26	1.49	direct
	edge-100S	1.51	0.21	indirect

on the 0S and 50S edges (the two-most stable edges) was simulated accordingly in order to probe their potential reactivity. Certainly these results are not complete in defining the catalytic or reactive nature of these edges, but could provide important insight on edge reactivity. H atom adsorption was modeled at various locations on the edges, either interacting with Sn or S atoms. There were several initial configurations with a single H adsorbed including a H atom on top of S, a H atom in between two Sn atoms, or a H atom in between two S atoms. Figure 3.12 shows the final configurations of the edges with H adsorbed. Reaction energies were calculated by

$$E_{ad} = E_H - E_{slab} - \frac{1}{2}E_{H_2}. \tag{3.16}$$

These results indicate that dissociative adsorption is weakest on the 0S edge, even more so than the basal planes. This may seem surprising, but adsorption over the 0S surface involves Sn-H bonds, while over the basal planes involves S-H bonds. S-H bonds are stronger than Sn-H bond, which explains these adsorption energies. Comparing with literatures, the hydrogen adsorption energy of SnS_2 edges is endothermic [33] although the accurate simulation of Gibbs free energy has not done yet. For comparison, hydrogen dissociative adsorption over MoS_2 was calculated to be exothermic[34, 35], which indicates that edges may have different properties for

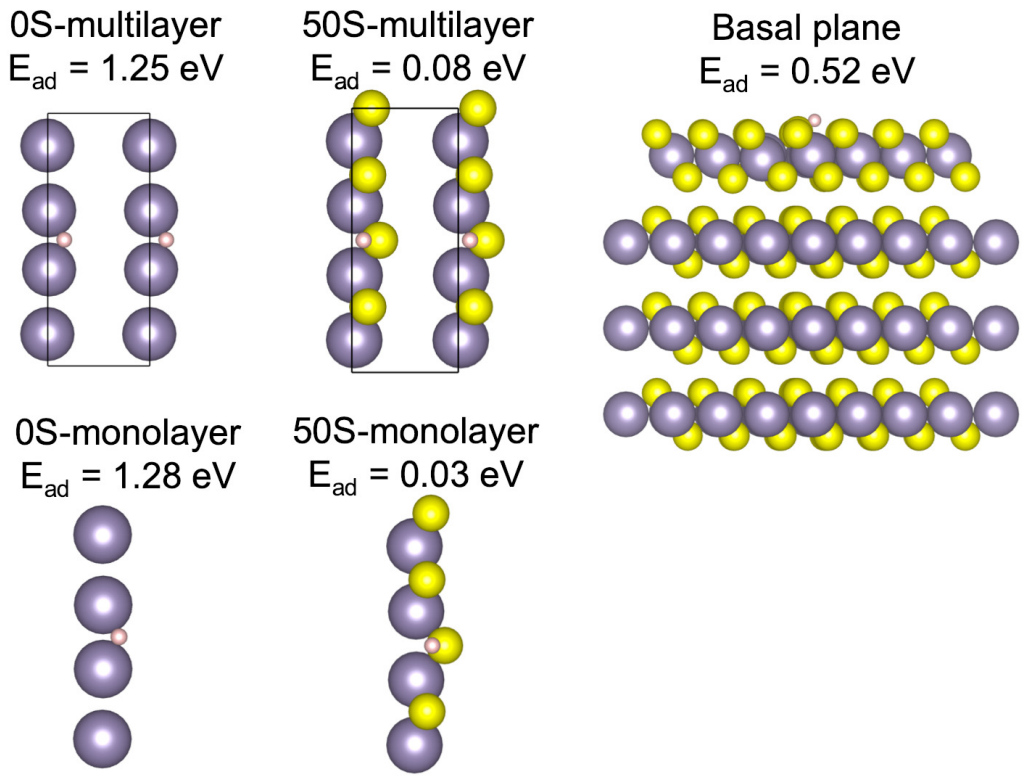

Figure 3.12: Hydrogen dissociative adsorption results on the 0S edges and 50S edges. Shown are the most stable configurations for adsorbed H atoms along with adsorption energies. For comparison, dissociative adsorption of H are given for the basal plane.

dichalcogenides. The results indicate that synthesis of SnS_2, especially under certain synthesis conditions, may form reactive flakes with edges that may be more reactive than basal planes. Such edges which may be key reaction sites. This may partially explain the experimental observations that edge-on oriented SnS_2 nanoflakes have better photoelectrochemical performance than single crystal SnS_2[20, 1].

3.6 Conclusion

Vertical SnS_2 nanoflakes were synthesized by close space sublimation (CSS). The nanoflakes have interesting stepped-layer structure and therefore contain more edges which are the active sites for catalytic reaction. Photocurrent as high as 4.5 mA cm^{-2} was achieved in aqueous phosphate buffer with Na_2SO_3, which is the highest photocurrent reported for any SnS_2 photoanode. To simulate the atomic structure and electronic structure of the edges of the SnS_2 nanoflakes, the $(10\bar{1}0)$ edges of both bulk-like and monolayer SnS_2 with different amount of S atoms were modeled by density functional theory (DFT). Thermodynamic analysis was also included to determine edge stability at different pressures and temperatures. The results show that 0S and 50S edges are most stable, and that higher S coverages are unstable. According to the thermodynamic calculation, the as-synthesized SnS_2 can have different edge terminations under different experimental condition, which means one can control terminations of SnS_2 edges by controlling experimental conditions. In contrast to the metallic edges of 2H-MoS_2 and WS_2, SnS_2 has semiconducting edges, indicating promising properties for photovoltaic and photocatalytic applications. The DFT work provides fundamental knowledge of bulk-like and monolayer SnS_2 edges including their atomic configurations and electronic structures, which is important for research and applications involving SnS_2.

Bibliography

[1] Binod Giri, Maryam Masroor, Tao Yan, Kateryna Kushnir, Alexander D Carl, Curtis Doiron, Haochuan Zhang, Yanyan Zhao, Arthur McClelland, Geoffrey A Tompsett, et al. Balancing light absorption and charge transport in vertical sns2 nanoflake photoanodes with stepped layers and large intrinsic mobility. *Advanced Energy Materials*, 9(31):1901236, 2019.

[2] Georg Kresse and Jürgen Hafner. Ab initio molecular dynamics for liquid metals. *Physical Review B*, 47(1):558, 1993.

[3] Georg Kresse and Jürgen Hafner. Ab initio molecular-dynamics simulation of the liquid-metal–amorphous-semiconductor transition in germanium. *Physical Review B*, 49(20):14251, 1994.

[4] Georg Kresse and Jürgen Furthmüller. Efficient iterative schemes for ab initio total-energy calculations using a plane-wave basis set. *Physical review B*, 54(16):11169, 1996.

[5] Georg Kresse and Jürgen Furthmüller. Efficiency of ab-initio total energy calculations for metals and semiconductors using a plane-wave basis set. *Computational materials science*, 6(1):15–50, 1996.

[6] John P Perdew, Kieron Burke, and Matthias Ernzerhof. Generalized gradient approximation made simple. *Physical review letters*, 77(18):3865, 1996.

[7] Jochen Heyd, Gustavo E Scuseria, and Matthias Ernzerhof. Hybrid functionals based on a screened coulomb potential. *The Journal of chemical physics*, 118(18):8207–8215, 2003.

[8] Stefan Grimme, Jens Antony, Stephan Ehrlich, and Helge Krieg. A consistent and accurate ab initio parametrization of density functional dispersion correction (dft-d) for the 94 elements h-pu. *The Journal of chemical physics*, 132(15):154104, 2010.

[9] Stefan Grimme, Stephan Ehrlich, and Lars Goerigk. Effect of the damping function in dispersion corrected density functional theory. *Journal of computational chemistry*, 32(7):1456–1465, 2011.

[10] Mengyi Li, Enzuo Liu, Huilin Hu, Shuxin Ouyang, Hua Xu, and Defa Wang. Surfactant-free synthesis of single crystalline sns2 and effect of surface atomic structure on the photocatalytic property. *International Journal of Photoenergy*, 2014, 2014.

[11] X-G Wang, Werner Weiss, Sh K Shaikhutdinov, Michael Ritter, Max Petersen, F Wagner, Robert Schlögl, and Matthias Scheffler. The hematite (α-fe 2 o 3)(0001) surface: evidence for domains of distinct chemistry. *Physical Review Letters*, 81(5):1038, 1998.

[12] Xiao-Gang Wang, Anne Chaka, and Matthias Scheffler. Effect of the environment on α- al 2 o 3 (0001) surface structures. *Physical Review Letters*, 84(16):3650, 2000.

[13] François Bottin, Fabio Finocchi, and Claudine Noguera. Stability and electronic structure of the (1$\times$ 1) srtio 3 (110) polar surfaces by first-principles calculations. *Physical Review B*, 68(3):035418, 2003.

[14] Dominic R Alfonso. Computational investigation of fes2 surfaces and prediction of effects of sulfur environment on stabilities. *The Journal of Physical Chemistry C*, 114(19):8971–8980, 2010.

[15] Karsten Reuter and Matthias Scheffler. Composition, structure, and stability of ruo 2 (110) as a function of oxygen pressure. *Physical Review B*, 65(3):035406, 2001.

[16] Beat Meyer. Elemental sulfur. *Chemical Reviews*, 76(3):367–388, 1976.

[17] Adam J Jackson, Davide Tiana, and Aron Walsh. A universal chemical potential for sulfur vapours. *Chemical science*, 7(2):1082–1092, 2016.

[18] KK Yee, RF Barrow, and Astri Rogstad. Resonance fluorescence and raman spectra of gaseous sulphur. *Journal of the Chemical Society, Faraday Transactions 2: Molecular and Chemical Physics*, 68:1808–1811, 1972.

[19] Malcom W Chase Jr and NIST-JANAF Thermochemical Tables. Data reported in nist standard reference database 69, june 2005 release: Nist chemistry webbook. *Journal of Physical and Chemical Reference Data, Monograph*, 9:1–1951, 1998.

[20] Guangbo Liu, Zhonghua Li, Tawfique Hasan, Xiaoshuang Chen, Wei Zheng, Wei Feng, Dechang Jia, Yu Zhou, and PingAn Hu. Vertically aligned two-dimensional sns 2 nanosheets with a strong photon capturing capability for efficient photoelectrochemical water splitting. *Journal of Materials Chemistry A*, 5(5):1989–1995, 2017.

[21] Yuan Huang, Eli Sutter, Jerzy T Sadowski, Mircea Cotlet, Oliver LA Monti, David A Racke, Mahesh R Neupane, Darshana Wickramaratne, Roger K Lake, Bruce A Parkinson, et al. Tin disulfide an emerging layered metal dichalcogenide semiconductor: Materials properties and device characteristics. *Acs Nano*, 8(10):10743–10755, 2014.

[22] Hongyan Shi, Rusen Yan, Simone Bertolazzi, Jacopo Brivio, Bo Gao, Andras Kis, Debdeep Jena, Huili Grace Xing, and Libai Huang. Exciton dynamics in suspended monolayer and few-layer mos2 2d crystals. *ACS nano*, 7(2):1072–1080, 2013.

[23] Thomas F Jaramillo, Kristina P Jørgensen, Jacob Bonde, Jane H Nielsen, Sebastian Horch, and Ib Chorkendorff. Identification of active edge sites for electrochemical h2 evolution from mos2 nanocatalysts. *science*, 317(5834):100–102, 2007.

[24] Lee A Burton, Thomas J Whittles, David Hesp, Wojciech M Linhart, Jonathan M Skelton, Bo Hou, Richard F Webster, Graeme O'Dowd, Christian Reece, David Cherns, et al. Electronic and optical properties of single crystal sns 2: an earth-abundant disulfide photocatalyst. *Journal of Materials Chemistry A*, 4(4):1312–1318, 2016.

[25] Yu Kumagai, Lee A Burton, Aron Walsh, and Fumiyasu Oba. Electronic structure and defect physics of tin sulfides: Sns, sn 2 s 3, and sn s 2. *Physical Review Applied*, 6(1):014009, 2016.

[26] Joseph M Gonzalez and Ivan I Oleynik. Layer-dependent properties of sns 2 and snse 2 two-dimensional materials. *Physical Review B*, 94(12):125443, 2016.

[27] Haichang Lu, Yuzheng Guo, and John Robertson. Band edge states, intrinsic defects, and dopants in monolayer hfs2 and sns2. *Applied Physics Letters*, 112(6):062105, 2018.

[28] Andrea Splendiani, Liang Sun, Yuanbo Zhang, Tianshu Li, Jonghwan Kim, Chi-Yung Chim, Giulia Galli, and Feng Wang. Emerging photoluminescence in monolayer mos2. *Nano letters*, 10(4):1271–1275, 2010.

[29] MV Bollinger, JV Lauritsen, Karsten Wedel Jacobsen, Jens Kehlet Nørskov, S Helveg, and Flemming Besenbacher. One-dimensional metallic edge states in mos2. *Physical Review Letters*, 87(19):196803, 2001.

[30] Yafei Li, Zhen Zhou, Shengbai Zhang, and Zhongfang Chen. Mos2 nanoribbons: high stability and unusual electronic and magnetic properties. *Journal of the American Chemical Society*, 130(49):16739–16744, 2008.

[31] Marco Bernardi, Maurizia Palummo, and Jeffrey C Grossman. Extraordinary sunlight absorption and one nanometer thick photovoltaics using two-dimensional monolayer materials. *Nano Letters*, 13(8):3664–3670, 2013.

[32] Meng-Lin Tsai, Sheng-Han Su, Jan-Kai Chang, Dung-Sheng Tsai, Chang-Hsiao Chen, Chih-I Wu, Lain-Jong Li, Lih-Juann Chen, and Jr-Hau He. Monolayer mos2 heterojunction solar cells. *ACS Nano*, 8(8):8317–8322, 2014.

[33] Xinyi Chia, Petr Lazar, Zdenek Sofer, Jan Luxa, and Martin Pumera. Layered sns versus sns2: valence and structural implications on electrochemistry and clean energy electrocatalysis. *The Journal of Physical Chemistry C*, 120(42):24098–24111, 2016.

[34] M. V. Bollinger, K. W. Jacobsen, and J. K. Nørskov. Atomic and electronic structure of mos_2 nanoparticles. *Physical Review B*, 67:085410, Feb 2003.

[35] Mingyong Sun, Alan E. Nelson, and John Adjaye. Adsorption and dissociation of h2 and h2s on mos2 and nimos catalysts. *Catalysis Today*, 105(1):36 – 43, 2005.

Chapter 4

Summary and Conclusions

To solve the energy crisis human being is facing now and in the future, the research work of renewable energy have to be speed up. Among all sustainable energies, hydrogen gas and solar energy are the two most clean and powerful ones. Water splitting is one common method to produce H_2 gas by reducing water. Two-dimensional (2D) materials, such as MoS_2, WS_2, and SnS_2 can be used in water splitting as catalysts to replace Pt, the best but also expensive catalyst. This thesis focuses on synthesis and property optimization of edge-on orientated 2D materials on photoelectrocatalysis performance.

Edge-on oriented WS_2 nanotubes were synthesized by sulfurization of chemical vapor deposition (CVD)-grown WO_x nanowires. However, the WS_2 nanotubes have been found did not have photoresponse. Since the crystal structure of WS_2 is the same as 2H-MoS_2, we also measured the photoelectrochemical (PEC) performance of CVD-grown MoS_2 vertical nanoflakes. As what was expected, vertical MoS_2 nanoflakes did not response to sun light either. One interesting known properties of MoS_2 edges is that the edges are metallic instead of semiconducting, which is the reason that it does not have photocurrent. DFT simulation found that the

edges of WS_2 are metallic too, just like the edges of MoS_2. The metallic edges can form continuous defect states in between the band gap which act like recombination trap state for photogenerated electrons, therefore the charge recombination rate at the metallic edges of WS_2 as well as MoS_2 is too high so that photocurrent of the materials is zero.

The SnS_2 vertical nanoflakes demonstrated that edge-on orientation of 2D materials is more efficient on charge transport than horizontal orientation, since the multi-layered structure is held by van der Waals interaction while within each layer the chemical bonds are holding the atoms together. Therefore the photogenerated electrons can transport within each layer more efficient than across layers. The photocurrent of our SnS_2 nanoflakes have as high as 4.5 mA cm^{-2} in phosphate buffer with 1 M Na_2SO_3 and 2.6 mA cm^{-2} in 0.5 M Na_2SO_4 which is around 1.7 times larger than CVD-grown vertical nanoflakes and almost 3 times larger than regular horizontal SnS_2 nanoflakes. This excellent photoelectrocatalysis performance is also from the unique stepped-layer structure of our SnS_2 nanoflakes which provide a lot more edges exposed and get involved in the catalytic reactions. Besides, we also proved that those edges are the active sites of SnS_2 nanoflakes.

Density functional theory (DFT) simulation shows that the edges of SnS_2 are still semiconductors with band gap energies slightly smaller than bulk SnS_2. Since the metallic edges form trap states inside the band gap leading to very high carrier recombination rate, the SnS_2 nanoflakes therefore has low carrier recombination rate. This explains why SnS_2 has the ability to achieve better PEC performance than MoS_2 and WS_2 do as mentioned above. During the simulation study, we found that the edges of both bulk-like and monolayer SnS_2 are covered by different amount of S atoms depends on synthesis conditions according to our thermodynamic calculation. At low pressure, i. e. in the high vacuum condition, the edges of SnS_2 are covered

by 0% of S atoms at relevant lower temperature, but 50% of S atoms are bonded at the edges at higher temperature. The more the S atoms at the edges, the smaller the band gap energies of the edges are. This suggests that we can control band gap energy of SnS_2 edges by controlling the synthesis parameters such as temperature and pressure.

All in all, edge-on orientated 2D materials is more efficient in charge transport than horizontal orientated ones. The metallic edges of MoS_2 and WS_2 are not ideal for PEC, because the metallic edges can form trap states inside the band gap leading to high carrier recombination rate. However, both MoS_2 and WS_2 can be used as electrocatalysis, in terms of which MoS_2 nanoflakes is better than WS_2 nanotubes due to the unexposed edges of the nanotubes. SnS_2 nanoflakes, on the other hand, has edge-rich stepped structure and the semiconducting edges, which therefore results in low carrier recombination rate and excellent performance on PEC water splitting.

Chapter 5

Future Recommendations

The high photoexcited carrier mobility of SnS_2 nanoflakes is a good factor for application of phototransistors. Monolayer MoS_2 was widely studied as phototransistors since the proper band gap energy (1.5 eV) and relatively high photoexcited carrier life time (0.1-1 ns). While the photoexcited carrier life time of CSS-grown SnS_2 nanoflakes were has high as 1.3 ns. In addition, the semiconducting edges of SnS_2 could avoid short circuit problem that MoS_2 transistors might have. Therefore, the SnS_2 nanoflakes should be very promising in phototransistors and even beyond the MoS_2. Similarly, SnS_2 nanoflakes could be a promising material for electron transport layer in solar cells [1] due to high carrier mobility and semiconducting edges.

To study deeper on H adsorption by density functional theory (DFT), it is better to simulate from 0% to 100% H adsorption at the edges and calculate Gibbs free energy. That way, the results can be compared with other water splitting materials such as MoS_2. Besides, the edge configurations of SnS_2 were simulated under high vacuum condition and S is the only element that was under consideration. In reality, the edges could be oxidized in the atmosphere. It would be more accurate and

interesting to model the edge oxidation and corrosion.

Bibliography

[1] Erling Zhao, Liguo Gao, Shuzhang Yang, Likun Wang, Junmei Cao, and Tingli Ma. In situ fabrication of 2d sns 2 nanosheets as a new electron transport layer for perovskite solar cells. *Nano Research*, 11(11):5913–5923, 2018.

Appendix A

Appendix 1: Density of states (DOS) of WS_2 edges

Density of states (DOS) of WS_2 edges are shown in Figure A.1. The middle two layers are also shown in each plot as reference, since the DOS of middle two layers are the same as the bulk WS_2. Because the DOS were simulated by PBE functional, the band gap energies of the middle two layers are smaller than the actual value (1.3 eV). The most of the edges are metallic, except 75W edges have band gap energies. According to table 2.1 the energies of 75W are relatively low, so these edges have little effect on the fact that the edges of WS_2 are metallic.

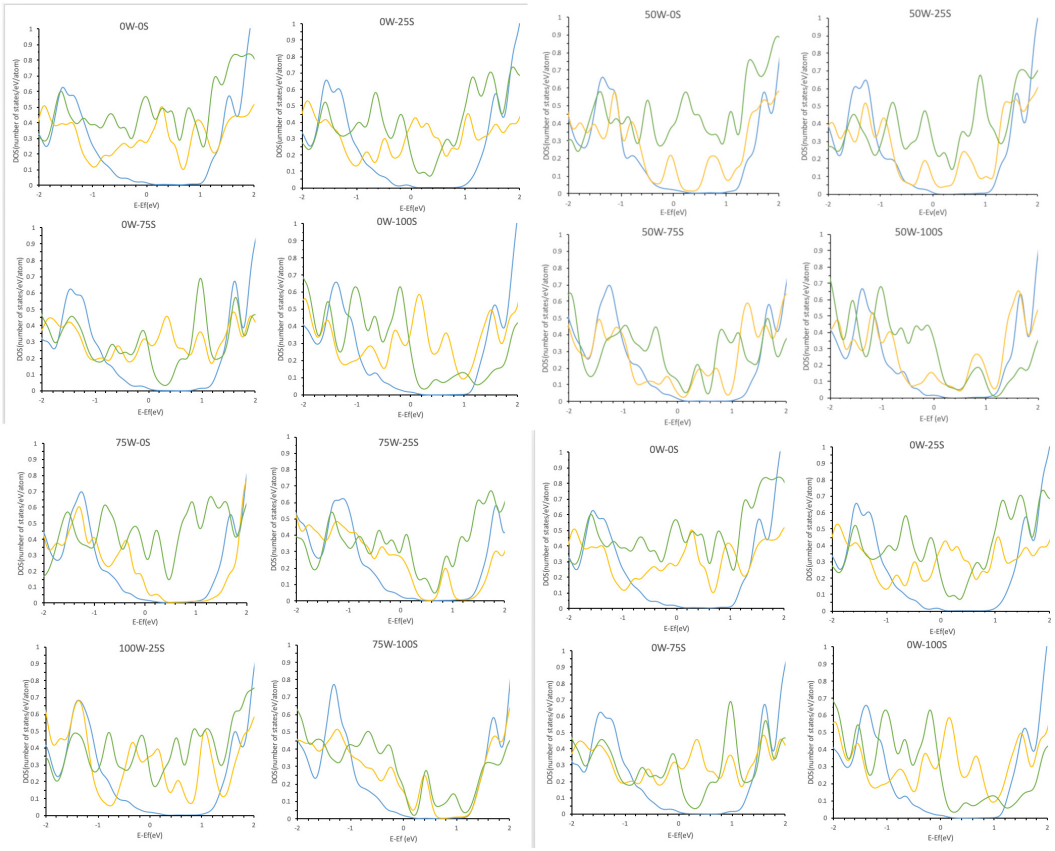

Figure A.1: Density of states of all converged WS_2 edges mentioned in chapter 2.3.4. Green curves are DOS of S edges, yellow curves are DOS of W edges, and blue curves represent DOS of middle two layers. The DOS of middle two layers should be the same as bulk WS_2 because of the slab model we used here. Note the DOS was simulated by PBE functional, therefore the band gap energies are smaller than their actual values.

Appendix B

Appendix 2: S_2 and S_8 chemical potential in different temperature and pressure

Table B.1 and B.2 tabulate the values of $\Delta\mu_S$ in eV at temperatures from 0 to 3000 K and pressure from 10^{-5} to 1 atm. All the data are obtained by equations:

$$\mu_S(T,p) = \mu_S(T,p^\circ) + \frac{1}{2}kTln(\frac{p}{p^\circ}), \tag{B.1}$$

where

$$\begin{aligned}\Delta\mu_S(T,p^\circ) &= \frac{1}{x}[H(T,p^\circ,S_2) - H(0K,p^\circ,S_2)] \\ &\quad -\frac{1}{x}T[S(T,p^\circ,S_2) - S(0K,p^\circ,S_2)].\end{aligned} \tag{B.2}$$

x equals to 2 or 8 for S_2 gas and S_8 gas, respectively. We used the JANAF thermochemical data[1] for entropy and enthalpy values used in Equation (B.2). This data was at 0.1 MPa, and used as the reference pressure p°.

Table B.1: $\Delta\mu_S$ values for S_2 gas at different temperatures and pressures. All numbers are in eV.

Temp (K)	10^{-5} atm	10^{-4} atm	10^{-3} atm	10^{-2} atm	10^{-1} atm	1 atm
0	0.00	0.00	0.00	0.00	0.00	0.00
100	-0.14	-0.13	-0.12	-0.11	-0.10	-0.09
200	-0.29	-0.27	-0.25	-0.23	-0.21	-0.19
300	-0.46	-0.43	-0.40	-0.37	-0.34	-0.31
400	-0.63	-0.59	-0.55	-0.51	-0.47	-0.43
500	-0.80	-0.75	-0.70	-0.65	-0.61	-0.56
600	-0.98	-0.92	-0.86	-0.80	-0.74	-0.69
700	-1.16	-1.10	-1.03	-0.96	-0.89	-0.82
723	-1.22	-1.15	-1.08	-1.01	-0.93	-0.86
800	-1.35	-1.27	-1.19	-1.11	-1.03	-0.95
900	-1.54	-1.45	-1.36	-1.27	-1.18	-1.09
1000	-1.73	-1.63	-1.53	-1.43	-1.33	-1.23
1500	-2.70	-2.55	-2.40	-2.25	-2.10	-1.96
2000	-3.71	-3.51	-3.31	-3.11	-2.91	-2.72
3000	-5.80	-5.50	-5.20	-4.90	-4.61	-4.31

Table B.2: $\Delta\mu_S$ values for S_8 gas at different temperatures and pressures. All numbers are in eV.

Temp (K)	10^{-5} atm	10^{-4} atm	10^{-3} atm	10^{-2} atm	10^{-1} atm	1 atm
0	0.00	0.00	0.00	0.00	0.00	0.00
100	-0.04	-0.04	-0.04	-0.04	-0.03	-0.03
200	-0.10	-0.09	-0.09	-0.08	-0.08	-0.07
300	-0.16	-0.16	-0.15	-0.14	-0.13	-0.13
400	-0.24	-0.23	-0.22	-0.21	-0.20	-0.19
500	-0.31	-0.30	-0.29	-0.28	-0.26	-0.25
600	-0.39	-0.38	-0.36	-0.35	-0.33	-0.32
700	-0.48	-0.46	-0.45	-0.43	-0.41	-0.39
723	-0.50	-0.48	-0.46	-0.45	-0.43	-0.41
800	-0.57	-0.55	-0.53	-0.51	-0.49	-0.47
900	-0.66	-0.64	-0.62	-0.59	-0.57	-0.55
1000	-0.75	-0.73	-0.70	-0.68	-0.66	-0.63
1500	-1.26	-1.22	-1.18	-1.15	-1.11	-1.07
2000	-1.80	-1.75	-1.70	-1.65	-1.60	-1.55
3000	-2.97	-2.89	-2.82	-2.74	-2.67	-2.60

Bibliography

[1] Malcom W Chase Jr and NIST-JANAF Thermochemical Tables. Data reported in nist standard reference database 69, june 2005 release: Nist chemistry webbook. *Journal of Physical and Chemical Reference Data, Monograph*, 9:1–1951, 1998.